Dynamic Modeling and Controller Design of Dual-Mode Cuk Inverter in Grid-Connected PV/TE Applications

Byeongcheol Han, *Student Member, IEEE*, Jih-Sheng Lai, *Fellow, IEEE*, and Minsung Kim, *Member, IEEE*

***Abstract*—This paper presents a dual-mode Cuk inverter for photovoltaic/thermoelectric power applications. A dual-mode Cuk inverter operates in both discontinuous conduction mode (DCM) and continuous conduction mode (CCM), and has the advantages of low ripples of voltage and current at the input and output, medium power density, and step-up/step-down ability, but is difficult to control because DCM and CCM have distinct system dynamics. To overcome this control problem, we propose to use a repetitive controller (RC) with a multiple phase-lead compensator for the dual-mode Cuk inverter. If the RC is applied by itself, the distinct system dynamics may severely degrade its system performance. Thus, in the proposed RC, we mainly use a multiple phase-lead compensator to compensate for the different phase lags of the dual-mode Cuk inverter. To reduce the burden from the RC, we use the dual-mode nominal duty ratio as feedforward control input. We also analyze the boundary of operation modes in the dual-mode Cuk inverter, then provide detailed and practical guidelines to design the control parameters. Experimental results obtained on a 500-W digitally controlled module integrated converter prototype confirmed the effectiveness of the control approach.**

***Index Terms*—Continuous conduction mode (CCM), discontinuous conduction mode (DCM), dual-mode nominal duty, fifth-order dynamic model, mode boundary, multiple phase-lead compensator, repetitive controller (RC), right-half-plane (RHP) zeros, unfolding-type inverter.**

I. Introduction

MODULE integrated converters (MICs) maximize energy harness from photovoltaic/thermoelectric (PV/TE) energy sources when there are mismatches between panels or cells, and offer "plug and play" characteristics [1], [2]. Of the single-phase MIC topologies available for PV/TE power systems [3]–[11], a Cuk inverter with unfolding circuit becomes more attractive for medium power PV/TE applications [12]–[15]. The existing MICs such as unfolding-type flyback inverters are more suitable for low-power applications due to the requirement of a large size magnetic component [16]. In addition, these circuits suffer from PV/TE output power fluctuation and grid harmonics so they usually adopt additional large size inductors to deal with these problems. In contrast, the unfolding-type Cuk inverter is able to use only one circuit to deliver medium power. Moreover, it shows low ripples of voltage and current at both input and output with potential cost saving because of its input/output inductors and capacitors [17]–[21]. This aspect differentiates the Cuk inverter from other MICs.

Cuk inverters can operate in discontinuous conduction mode (DCM) or continuous conduction mode (CCM). A Cuk inverter that operates in DCM can be used in medium to low power applications. In DCM, the switch is turned ON at almost-zero current and the output diode is turned OFF at almost-zero current. Thus, the power conversion efficiency is relatively high at the medium to low rated power [22]–[25]. However, as the power capacity of PV/TE modules is increased [26], [27], the penalty with a relatively higher conduction loss and switching turn-off loss prevents it from being practical due to high peak current [19], [25]. Thus, the use of the Cuk DCM inverter is limited to the medium to low power range ($\leq$300 W) [19]. For applications higher than 300-W power level, the Cuk inverter must operate in CCM to lower current stress. However, it requires large input and output inductors.

To attain medium to high power capacity with a given size of input and output inductors, the Cuk inverter must be able to operate in either DCM or CCM (dual mode). It operates in DCM at low instantaneous power level in a grid period, and in CCM at high instantaneous power level in that. Thus, it achieves both high efficiency and compact size at medium to high power. However, it does have an output current control problem; in DCM, the system dynamics is relatively weak due to the large right-half-plane (RHP) zeros in its transfer function, but the system gain is low. In contrast, in CCM, the system gain is relatively high but is seriously affected by a very small RHP zero, which creates negative phase shift at low frequency and limits the available controller bandwidth [28]. In addition, the dual-mode Cuk inverter is badly affected by grid voltage

Manuscript received July 26, 2017; revised October 17, 2017; accepted November 29, 2017. Date of publication December 4, 2017; date of current version July 15, 2018. This work was supported in part by the Ministry of Science, ICT, and Future Planning (MSIP) supervised by the Institute for Information & Communications Technology Promotion (IITP), South Korea, under the "ICT Consilience Creative Program" (IITP-R0346-16-1007) and in part by the National Research Foundation of Korea Grant funded by the MSIP (2017R1C1B1003084). Recommended for publication by Associate Editor M. A. E. Andersen. *(Corresponding author: Minsung Kim.)*

B. Han is with the Department of Creative IT Engineering, Pohang University of Science and Technology (POSTECH), Pohang 37673, South Korea (e-mail: hbychol@postech.ac.kr).

J.-S. Lai is with the Future Energy Electronics Center, Virginia Polytechnic Institute and State University (Virginia Tech), Blacksburg, VA 24061 USA (e-mail: laijs@vt.edu).

M. Kim is with the Division of Electronics and Electrical Engineering, Dongguk University, Seoul, 04620, Korea (e-mail: mail.minsung.kim@gmail.com).

Color versions of one or more of the figures in this paper are available online at http://ieeexplore.ieee.org.

Digital Object Identifier 10.1109/TPEL.2017.2779843

disturbance when connected to an utility grid [29], [30]. The different system dynamics and the grid disturbance can cause the dual-mode Cuk inverter system to become unstable when the circuit is combined with conventional feedback controller.

In this paper, to overcome the control problems, we propose the use of repetitive controller (RC) with a multiple phase-lead compensator for the dual-mode Cuk inverter. The RC algorithm is an effective solution to track a periodic reference current and to eliminate periodic grid disturbances in dynamic systems. It repetitively adjusts the current control inputs by analyzing the information obtained from the previous trial, and consequently generates a series of control inputs such that the tracking errors converge to zero [31]–[35]. However, if the RC is applied by itself, its system performance can be severely degraded by the distinct system dynamics in DCM and CCM. Thus, in the proposed RC, we mainly use the multiple phase-lead compensator to compensate for the phase lag of the dual-mode Cuk inverter. To reduce the burden from the RC, we use the dual-mode nominal duty ratio as the feedforward control input. We also analyze the boundary of operation modes in dual-mode Cuk inverter. Then, we present detailed and practical guidelines to the design of the control parameters. Experimental results verify that the proposed control scheme achieves desirable performance. The key contributions of this paper are as follows.

1) A dual-mode Cuk inverter is first developed for grid-connected PV/TE power applications.
2) Compared to the existing control schemes, the proposed control scheme can significantly improve the steady-state response of the dual-mode Cuk inverter under the different system dynamics and the grid voltage disturbance.
3) Dynamic modeling of the dual-mode Cuk inverter has been conducted and used to design the control parameters.

This paper is organized as follows. The dynamic modeling of dual-mode Cuk inverter is described in Section II, a control scheme is proposed for dual-mode Cuk inverter in Section III. In Section IV, experimental setup and results are presented. Conclusions are drawn in Section V.

II. Dynamic Modeling of Dual-Mode Cuk Inverter

The unfolding-type Cuk inverter [see Fig. 1(a)] consists of inductor L_1, primary switch S_1, capacitor C_1, ideal transformer T with turns ratio $n = N_s/N_p$, capacitor C_2, diode D_1, inductor L_2, capacitor C_3, unfolding bridge (S_2–S_5), and output inductor L_f. v_{in} is the input voltage, and $|v_g|$ is the rectified grid voltage. The Cuk converter with rectified output is a part of the unfolding-type Cuk inverter that transforms dc input into rectified sinusoidal output current with the line frequency. Then, the unfolding circuit changes alternate halves of the sinusoidal shape to yield a full-sinusoidal waveform.

Fig. 1(b) shows the equivalent circuit of the unfolding-type Cuk inverter. Note that internal resistances of C_3 and L_f are considered only in Fig. 1(b), because internal resistances of C_3 and L_f add one left-half-plane (LHP) zero in the transfer function of the Cuk inverter, but other internal resistances have no significant impact on the system dynamics [36]. This circuit operates with three phases per switching period: first, S_1 turned ON and D_1 turned OFF; second, S_1 turned OFF and D_1 turned ON; third, S_1 turned OFF and D_1 turned OFF. When S_1 is turned ON and D_1 is turned OFF [see Fig. 2(a)], the current flowing through L_1 increases, and L_1 stores energy. C_1 is discharged, and T transmits the energy to the secondary part of the circuit. C_2 is also discharged and the energy is transmitted to the output stage formed by L_2, C_3, and L_f. When S_1 is turned OFF and D_1 is turned ON [see Fig. 2(b)], the currents of both L_1 and L_2 decrease, and C_1 and C_2 are charged due to the energy stored in L_1. In CCM, the operation of the circuit returns to the first phase, but in DCM, the currents through both L_1 and L_2 decrease, so the current through L_2 becomes negative; even though the current flows through L_2 in the negative direction, D_1 is not turned OFF because the current still flows through it. When current i_{D_1} reaches zero [see Fig. 2(c)], D_1 is turned OFF and the current i_{L_2} passes through only C_2 not D_1; as a result, a Cuk inverter operating in DCM will have dc offset currents I_X and I_X/n (see Fig. 3) unlike other converters in DCM [22]–[25].

For a given average magnetizing current, the Cuk inverter requires less peak current when operating in CCM than in DCM (see Fig. 3), and thus achieving a higher efficiency in CCM. As the inductances of L_1 and L_2 increase, the CCM region widens in a single grid period, thereby increasing the power conversion efficiency, but this strategy requires the increase of inductor size. Therefore, the inductances must be carefully chosen to provide both high efficiency and compact size.

The state-space equations of the three operating phases are as follows:

Phase 1 (S_1 ON, D_1 OFF)

$$\begin{bmatrix} \frac{di_{L_1}(t)}{dt} \\ \frac{di_{L_2}(t)}{dt} \\ \frac{dv_{C_{12}}(t)}{dt} \\ \frac{dv_{C_3}(t)}{dt} \\ \frac{di_{L_f}(t)}{dt} \end{bmatrix} = \begin{bmatrix} 0 & 0 & 0 & 0 & 0 \\ 0 & -\frac{R_{C_3}}{L_2} & \frac{1}{L_2} & -\frac{1}{L_2} & \frac{R_{C_3}}{L_2} \\ 0 & -\frac{1}{C_{12}} & 0 & 0 & 0 \\ 0 & \frac{1}{C_3} & 0 & 0 & -\frac{1}{C_3} \\ 0 & \frac{R_{C_3}}{L_f} & 0 & \frac{1}{L_f} & -\frac{R_{C_3}+R_f}{L_f} \end{bmatrix} \cdot \begin{bmatrix} i_{L_1}(t) \\ i_{L_2}(t) \\ v_{C_{12}}(t) \\ v_{C_3}(t) \\ i_{L_f}(t) \end{bmatrix} + \begin{bmatrix} \frac{1}{L_1} & 0 \\ 0 & 0 \\ 0 & 0 \\ 0 & 0 \\ 0 & -\frac{1}{L_f} \end{bmatrix} \cdot \begin{bmatrix} v_{\text{in}}(t) \\ |v_g(t)| \end{bmatrix} \quad (1)$$

Phase 2 (S_1 OFF, D_1 ON)

$$\begin{bmatrix} \frac{di_{L_1}(t)}{dt} \\ \frac{di_{L_2}(t)}{dt} \\ \frac{dv_{C_{12}}(t)}{dt} \\ \frac{dv_{C_3}(t)}{dt} \\ \frac{di_{L_f}(t)}{dt} \end{bmatrix} = \begin{bmatrix} 0 & 0 & -\frac{1}{nL_1} & 0 & 0 \\ 0 & -\frac{R_{C_3}}{L_2} & 0 & -\frac{1}{L_2} & \frac{R_{C_3}}{L_2} \\ \frac{1}{nC_{12}} & 0 & 0 & 0 & 0 \\ 0 & \frac{1}{C_3} & 0 & 0 & -\frac{1}{C_3} \\ 0 & \frac{R_{C_3}}{L_f} & 0 & \frac{1}{L_f} & -\frac{R_{C_3}+R_f}{L_f} \end{bmatrix} \cdot \begin{bmatrix} i_{L_1}(t) \\ i_{L_2}(t) \\ v_{C_{12}}(t) \\ v_{C_3}(t) \\ i_{L_f}(t) \end{bmatrix} + \begin{bmatrix} \frac{1}{L_1} & 0 \\ 0 & 0 \\ 0 & 0 \\ 0 & 0 \\ 0 & -\frac{1}{L_f} \end{bmatrix} \cdot \begin{bmatrix} v_{\text{in}}(t) \\ |v_g(t)| \end{bmatrix} \quad (2)$$

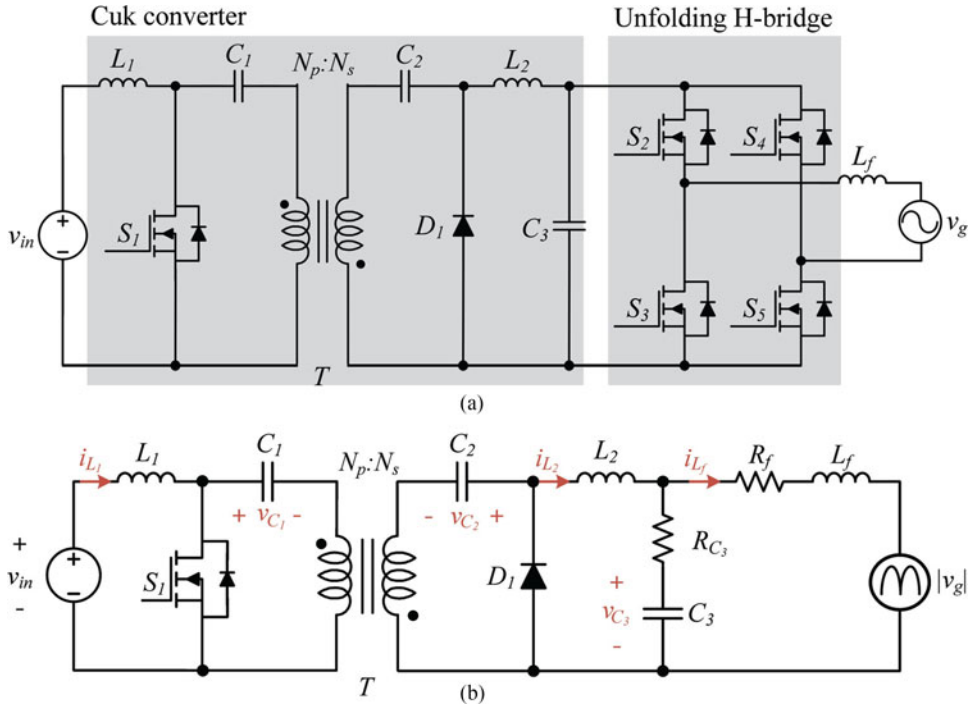

Fig. 1. Circuit diagram of the unfolding-type Cuk inverter. Components are described in the text. (a) Block diagram. (b) Equivalent circuit.

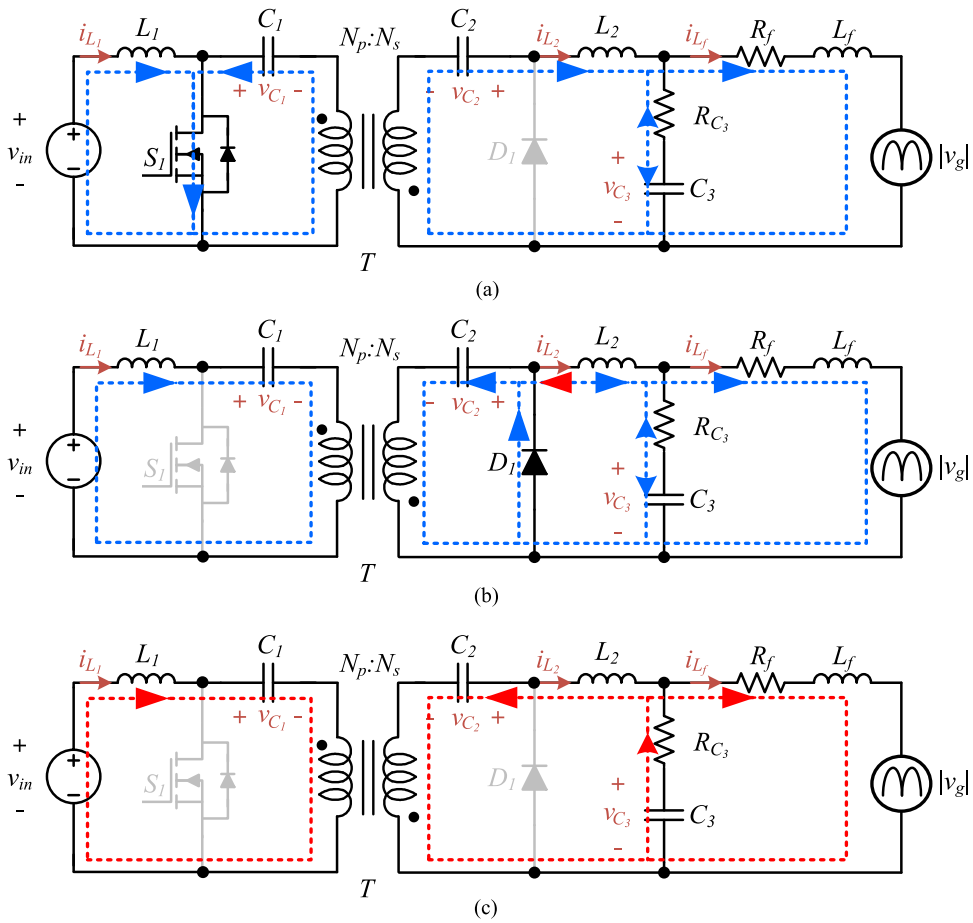

Fig. 2. Operating modes of the unfolding-type Cuk inverter; current flow in DCM and CCM (blue); additional current flow in DCM (red). (a) Phase 1 (S_1 ON, D_1 OFF, in DCM and CCM). (b) Phase 2 (S_1 OFF, D_1 ON, in DCM and CCM). (c) Phase 3 (S_1 OFF, D_1 OFF, in DCM).

Phase 3 (S_1 OFF, D_1 OFF)

$$\begin{bmatrix} \frac{di_{L_1}(t)}{dt} \\ \frac{di_{L_2}(t)}{dt} \\ \frac{dv_{C_{12}}(t)}{dt} \\ \frac{dv_{C_3}(t)}{dt} \\ \frac{di_{L_f}(t)}{dt} \end{bmatrix} = \begin{bmatrix} -\frac{R_{C_3}}{n^2L_{12}} & 0 & -\frac{1}{L_{12}} & \frac{1}{nL_{12}} & -\frac{R_{C_3}}{nL_{12}} \\ 0 & -\frac{R_{C_3}}{n^2L_{12}} & \frac{1}{n^2L_{12}} & -\frac{1}{n^2L_{12}} & \frac{R_{C_3}}{n^2L_{12}} \\ \frac{1}{nC_{12}} & 0 & 0 & 0 & 0 \\ 0 & \frac{1}{C_3} & 0 & 0 & -\frac{1}{C_3} \\ 0 & \frac{R_{C_3}}{L_f} & 0 & \frac{1}{L_f} & -\frac{R_{C_3}+R_f}{L_f} \end{bmatrix} \cdot \begin{bmatrix} i_{L_1}(t) \\ i_{L_2}(t) \\ v_{C_{12}}(t) \\ v_{C_3}(t) \\ i_{L_f}(t) \end{bmatrix} + \begin{bmatrix} \frac{1}{L_{12}} & 0 \\ -\frac{1}{nL_{12}} & 0 \\ 0 & 0 \\ 0 & 0 \\ 0 & -\frac{1}{L_f} \end{bmatrix} \cdot \begin{bmatrix} v_{\text{in}}(t) \\ |v_g(t)| \end{bmatrix} \tag{3}$$

where $i_{L_1}(t)$, $i_{L_2}(t)$, and $i_{L_f}(t)$ are, respectively, the currents flowing through L_1, L_2, and L_f; $v_{C_{12}}(t) = nv_{C_1}(t) + v_{C_2}(t)$, where $v_{C_1}(t)$ and $v_{C_2}(t)$ are, respectively, the voltages across C_1 and C_2; $L_{12} = L_1 + L_2/n^2$; $C_{12} = (C_1C_2)/(C_1 + n^2C_2)$; $v_{C_3}(t)$ is the voltage across C_3, R_f is the parasitic resistance of L_f, and R_{C_3} is the parasitic resistance of C_3.

The Cuk inverter undergoes phases 1, 2, and 3 in DCM, but only phases 1 and 2 in CCM. Using the state-space averaging method, we derive the average model as follows where $\mathbf{x}(t) = [i_{L_1}(t), i_{L_2}(t), v_{C_{12}}(t), v_{C_3}(t), i_{L_f}(t)]^T$ is the state vector, $y(t) = i_{L_f}(t)$ is the output, $d_1(t)$ is the duty ratio, $d_2(t) = \frac{2(i_{L_1}(t)+ni_{L_2}(t))L_1L_2}{d_1(t)T_s(L_2v_{\text{in}}(t)+L_1n(v_{C_{12}}(t)-v_{C_3}(t))} - d_1(t)$ in DCM, $d_2(t) = 1 - d_1(t)$ in CCM, and $M(t) = \frac{1-d_1(t)-d_2(t)}{L_{12}}$.

Linearizing the average model (4) and (5) shown at the bottom of this page, yields the small-signal models for DCM and CCM as follows.

DCM

$$\dot{\hat{\mathbf{x}}}(t) = \begin{bmatrix} \frac{\partial F_1}{\partial \hat{x}_1} & \frac{\partial F_1}{\partial \hat{x}_2} & \frac{\partial F_1}{\partial \hat{x}_3} & \frac{\partial F_1}{\partial \hat{x}_4} & \frac{\partial F_1}{\partial \hat{x}_5} \\ \frac{\partial F_2}{\partial \hat{x}_1} & \frac{\partial F_2}{\partial \hat{x}_2} & \frac{\partial F_2}{\partial \hat{x}_3} & \frac{\partial F_2}{\partial \hat{x}_4} & \frac{\partial F_2}{\partial \hat{x}_5} \\ \frac{1-D}{n^2C_{12}} & -\frac{D}{C_{12}} & 0 & 0 & 0 \\ 0 & \frac{1}{C_3} & 0 & 0 & -\frac{1}{C_3} \\ 0 & \frac{R_{C_3}}{L_f} & 0 & \frac{1}{L_f} & -\frac{R_{C_3}+R_f}{L_f} \end{bmatrix} \hat{\mathbf{x}}(t) + \begin{bmatrix} \frac{\partial F_1}{\partial \hat{d}} \\ \frac{\partial F_2}{\partial \hat{d}} \\ -\frac{I_{L_1}}{n^2C_{12}} - \frac{I_{L_2}}{C_{12}} \\ 0 \\ 0 \end{bmatrix} \hat{d}(t) \tag{6}$$

$$\hat{y}(t) = \begin{bmatrix} 0 & 0 & 0 & 0 & 1 \end{bmatrix} \hat{\mathbf{x}}(t). \tag{7}$$

CCM

$$\dot{\hat{\mathbf{x}}}(t) = \begin{bmatrix} 0 & 0 & -\frac{1-D}{nL_1} & 0 & 0 \\ 0 & -\frac{R_{C_3}}{L_2} & \frac{D}{L_2} & -\frac{1}{L_2} & \frac{R_{C_3}}{L_2} \\ \frac{1-D}{n^2C_{12}} & -\frac{D}{C_{12}} & 0 & 0 & 0 \\ 0 & \frac{1}{C_3} & 0 & 0 & -\frac{1}{C_3} \\ 0 & \frac{R_{C_3}}{L_f} & 0 & \frac{1}{L_f} & -\frac{R_{C_3}+R_f}{L_f} \end{bmatrix} \hat{\mathbf{x}}(t) + \begin{bmatrix} \frac{V_{C_{12}}}{nL_1} \\ \frac{V_{C_{12}}}{L_2} \\ -\frac{I_{L_1}}{n^2C_{12}} - \frac{I_{L_2}}{C_{12}} \\ 0 \\ 0 \end{bmatrix} \hat{d}(t) \tag{8}$$

$$\hat{y}(t) = \begin{bmatrix} 0 & 0 & 0 & 0 & 1 \end{bmatrix} \hat{\mathbf{x}}(t) \tag{9}$$

$$\dot{\mathbf{x}}(t) = \begin{bmatrix} -\frac{R_{C_3}M(t)}{n^2} & 0 & -\frac{d_2(t)}{nL_1} - M(t) & \frac{M(t)}{n} & -\frac{R_{C_3}M(t)}{n} \\ 0 & -\frac{R_{C_3}(d_1(t)+d_2(t))}{L_2} - \frac{R_{C_3}M(t)}{n^2} & \frac{d_1(t)}{L_2} + \frac{M(t)}{n^2} & -\frac{d_1(t)+d_2(t)}{L_2} - \frac{M(t)}{n^2} & \frac{R_{C_3}(d_1(t)+d_2(t))}{L_2} + \frac{R_{C_3}M(t)}{n^2} \\ \frac{1-d_1(t)}{nC_{12}} & -\frac{d_1(t)}{C_{12}} & 0 & 0 & 0 \\ 0 & \frac{1}{C_3} & 0 & 0 & -\frac{1}{C_3} \\ 0 & \frac{R_{C_3}}{L_f} & 0 & \frac{1}{L_f} & -\frac{R_{C_3}+R_f}{L_f} \end{bmatrix} \mathbf{x}(t) + \begin{bmatrix} \frac{d_1(t)+d_2(t)}{L_1} + M(t) & 0 \\ -\frac{M(t)}{n} & 0 \\ 0 & 0 \\ 0 & 0 \\ 0 & -\frac{1}{L_f} \end{bmatrix} \cdot \begin{bmatrix} v_{\text{in}}(t) \\ |v_g(t)| \end{bmatrix} \tag{4}$$

$$y(t) = \begin{bmatrix} 0 & 0 & 0 & 0 & 1 \end{bmatrix} \mathbf{x}(t) \tag{5}$$

where $\hat{\mathbf{x}}(t) = [\hat{i}_{L_1}(t), \hat{i}_{L_2}(t), \hat{v}_{C_{12}}(t), \hat{v}_{C_3}(t), \hat{i}_{L_f}(t)]^T$ and $\hat{y}(t) = \hat{i}_{L_f}(t)$ are, respectively, the incremental variations of $\mathbf{x}(t)$ and $y(t)$. $\hat{i}_{L_1}(t)$, $\hat{i}_{L_2}(t)$, $\hat{v}_{C_{12}}(t)$, $\hat{v}_{C_3}(t)$, $\hat{i}_{L_f}(t)$, and $\hat{d}(t)$ are, respectively, the incremental variations of $i_{L_1}(t)$, $i_{L_2}(t)$, $v_{C_{12}}(t)$, $v_{C_3}(t)$, $i_{L_f}(t)$, and $d_1(t)$, and I_{L_1}, I_{L_2}, $V_{C_{12}}$, V_{C_3}, I_{L_f}, and D are, respectively, the values at the operating point of $i_{L_1}(t)$, $i_{L_2}(t)$, $v_{C_{12}}(t)$, $v_{C_3}(t)$, $i_{L_f}(t)$, and $d_1(t)$. F_i, $\frac{\partial F_i}{\partial \hat{x}_j}$, and $\frac{\partial F_i}{\partial \hat{d}}$ for $i = 1, 2$ and $j = 1, \ldots, 5$ are defined in Appendix A.

Based on these small-signal models for DCM and CCM, the transfer functions from the control input to the output can be obtained as follows:

DCM

$$G_{\text{id\_DCM}}(s) = \frac{\hat{i}_{L_f}(s)}{\hat{d}(s)} = \frac{a_1 s^3 + a_2 s^2 + a_3 s + a_4}{b_1 s^5 + b_2 s^4 + b_3 s^3 + b_4 s^2 + b_5 s + b_6} \tag{10}$$

CCM

$$G_{\text{id\_CCM}}(s) = \frac{\hat{i}_{L_f}(s)}{\hat{d}(s)} = \frac{c_1 s^3 + c_2 s^2 + c_3 s + c_4}{e_1 s^5 + e_2 s^4 + e_3 s^3 + e_4 s^2 + e_5 s + e_6} \tag{11}$$

where the derived parameters a_i and c_i for $i = 1, \ldots, 4$ and b_j and e_j for $j = 1, \ldots, 6$ are given in Appendix A. Analysis of the small-signal models for DCM and CCM shows two RHP zeros, one LHP zero and five LHP poles.

To design the controller in the discrete-time domain, we must derive the small-signal models in the discrete-time domain. Using the backward difference method [37] with the switching period T_s, we can obtain the discrete-time transfer functions as follows:

DCM

$$G_{\text{id\_DCM}}(z) = \frac{\hat{i}_{L_f}(z)}{\hat{d}(z)} = \frac{f_1 z^5 + f_2 z^4 + f_3 z^3 + f_4 z^2}{g_1 z^5 + g_2 z^4 + g_3 z^3 + g_4 z^2 + g_5 z + g_6} \tag{12}$$

CCM

$$G_{\text{id\_CCM}}(z) = \frac{\hat{i}_{L_f}(z)}{\hat{d}(z)} = \frac{l_1 z^5 + l_2 z^4 + l_3 z^3 + l_4 z^2}{m_1 z^5 + m_2 z^4 + m_3 z^3 + m_4 z^2 + m_5 z + m_6} \tag{13}$$

where the parameters f_i and l_i for $i = 1, \ldots, 4$ and g_j and m_j for $j = 1, \ldots, 6$ are given in Appendix B.

III. Control Strategy of Dual-Mode Cuk Inverter

The objective of controlling the dual-mode Cuk inverter is to make the output current track the desired sinusoidal signal as closely as possible. To stabilize the dual-mode Cuk inverter, we can use a conventional proportional–integral (PI) controller. The transfer functions of PI controllers in DCM and CCM regions are as follows:

$$C_{\text{fb\_DCM}}(z) = k_{p\_\text{DCM}} + k_{i\_\text{DCM}} \frac{T_s}{1 - z^{-1}} \tag{14}$$

$$C_{\text{fb\_CCM}}(z) = k_{p\_\text{CCM}} + k_{i\_\text{CCM}} \frac{T_s}{1 - z^{-1}} \tag{15}$$

where k_{p_DCM} and k_{i_DCM} are the proportional and integral controller gains in DCM, and k_{p_CCM} and k_{i_CCM} are the proportional and integral controller gains in CCM.

However, the conventional PI controller cannot satisfy the desired control performance due to the different system dynamics in dual-mode Cuk inverter and the grid disturbance. In DCM, the effect of system dynamics is relatively weak due to the large RHP zeros, but the system gain is very low. In CCM, the system gain is relatively high but it has a much smaller RHP zero than those in DCM. This small RHP zero creates negative phase shift at lower frequency and limits the available controller bandwidth [28]. This circuit also suffers from the grid disturbance when it operates when connected to a utility grid [29], [30]. To overcome these problems, we propose to use an RC with a multiple phase-lead compensator. To reduce the burden from the RC, we use the dual-mode nominal duty ratio as feedforward control input. In this section, we first construct the nominal duty ratio with boundary of the operation modes; then, we develop an RC with a multiple phase-lead compensator.

A. Nominal Duty Ratio of Dual-Mode Cuk Inverter

At the operating points of DCM/CCM, the grid voltage and the input voltage change much more slowly than the inductor currents i_{L_1} and i_{L_2}. We can then assume that the inverter operates in quasi-steady state during the switching period. Assuming that the Cuk inverter is lossless, the power-balance equations under DCM/CCM regions are obtained as follows:

$$V_{\text{in}} I_{\text{in}} = V_{\text{rms}} I_{\text{rms}} = P_o \tag{16}$$

$$V_{\text{in}} \bar{I}_{L_1} = V_g I_g = 2 V_{\text{rms}} I_{\text{rms}} \sin^2 wt \tag{17}$$

where V_{in} is the average input voltage over a switching cycle, I_{in} is the average input current over a switching cycle, V_{rms} is the RMS value of the grid voltage, I_{rms} is the RMS value of the grid current, P_o is the output power, $\bar{I}_{L_1}$ is the average current through L_1 over a switching cycle, V_g is the average grid voltage over a switching cycle, I_g is the average grid current over a switching cycle, and w is the angular frequency of the grid voltage.

Based on waveforms of the Cuk inverter operating in DCM [see Fig. 3(a)], the average currents $\bar{I}_{L_1}$ and $\bar{I}_{L_2}$ can be represented as follows:

$$\bar{I}_{L_1} = \frac{V_{\text{in}} d_1 T_s}{2 L_1} (d_1 + d_2) + I_X \tag{18}$$

$$\bar{I}_{L_2} = \frac{V_{C_3} d_2 T_s}{2 L_2} (d_1 + d_2) - I_X / n = \frac{n V_{\text{in}} d_1 T_s}{2 L_2} (d_1 + d_2) - I_X / n. \tag{19}$$

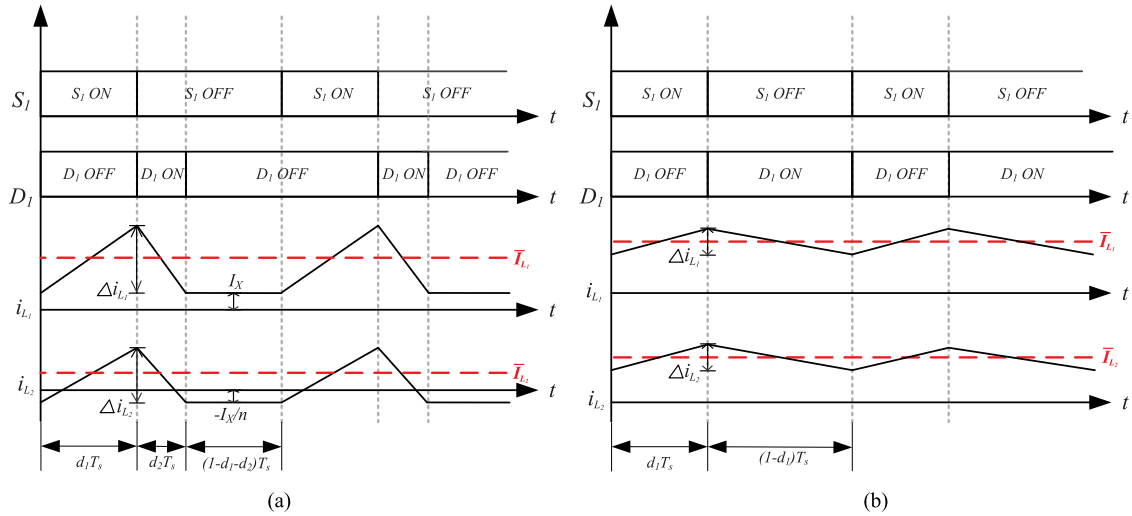

Fig. 3. The current waveforms of the inductor currents i_{L_1} and i_{L_2} corresponding to S_1 and D_1 states. T_s: the switching period of switch S_1. d_1: turn-on duty ratio. d_2: falling duty ratio. I_X: dc offset current. $\bar{I}_{L_1}$: average current through L_1. $\bar{I}_{L_2}$: average current through L_2. (a) In DCM. (b) In CCM.

To neglect the effect of I_X, we first add $n\bar{I}_{L_2}$ to $\bar{I}_{L_1}$. Then, we have the following:

$$\bar{I}_{L_1} + n\bar{I}_{L_2} = \frac{V_{\text{in}} d_1 T_s}{2}(d_1 + d_2)\left(\frac{1}{L_1} + \frac{n^2}{L_2}\right). \tag{20}$$

Applying the current-second balance law to the capacitors C_1 and C_2, the relationship between $\overline{I}_{L_1}$ and $\overline{I}_{L_2}$ can be obtained as follows:

$$n\overline{I}_{L_2} = \frac{d_2}{d_1}\overline{I}_{L_1}. \tag{21}$$

Substituting (21) into (20) yields the following:

$$\bar{I}_{L_1} = \frac{V_{\text{in}} d_1^2 T_s}{2L_{\text{eq}}} \tag{22}$$

where $L_{\text{eq}} = L_1 L_2/(n^2 L_1 + L_2)$.

Substituting (22) into (17) yields the nominal duty ratio in DCM as follows:

$$\begin{aligned} D_{\text{DCM}}(t) &= \sqrt{\frac{2L_{\text{eq}}|V_g||I_g|}{V_{\text{in}}^2 T_s}} \\ &= \sqrt{\frac{4L_{\text{eq}} V_{\text{rms}} I_{\text{rms}} \sin^2 \omega t}{V_{\text{in}}^2 T_s}} \\ &= \frac{2}{V_{\text{in}}}\sqrt{\frac{L_{\text{eq}} P_o}{T_s}}|\sin \omega t|. \end{aligned} \tag{23}$$

When the Cuk inverter operates in CCM, the nominal duty ratio can be obtained by using the voltage-second balance law. Disregarding the parasitic resistors R_f and R_{C_3} and using the voltage-second balance for the inductors (L_1, L_2, and L_f) over a switching period T_s, we can derive

$$V_{\text{in}} - (1 - D)\left(V_{C_1} + \frac{1}{n}V_{C_2}\right) = 0 \tag{24}$$

$$D(nV_{C_1} + V_{C_2}) - V_{C_3} = 0 \tag{25}$$

$$V_{C_3} - |V_g| = 0 \tag{26}$$

Combining (24)–(26) yields the nominal duty ratio in CCM D_{CCM} as

$$D_{\text{CCM}}(t) = \frac{|V_g|}{nV_{\text{in}} + |V_g|}. \tag{27}$$

B. Boundary of the Operation Modes

Fig. 4 illustrates the dual-mode Cuk inverter operating in DCM and CCM. It operates in DCM at low instantaneous power level. As the instantaneous power level increases, it starts to operate in CCM. In DCM, i_{L_1} shows positive dc offset current I_X and i_{L_2} shows negative dc offset current I_X/n. This dc offset current differentiates the Cuk inverter operating in DCM from other DCM inverters.

The Cuk inverter can be classified into DCM and CCM by comparing the dc component of inductor current and the halves of inductor current ripple (see Fig. 3). Here, the dc offset current I_X complicates the problem of solving the inequality. Thus, instead of comparing $\overline{I}_{L_1}$ and $\triangle i_{L_1}$ or $\overline{I}_{L_2}$ and $\triangle i_{L_2}$, we compared $\overline{I}_{L_1} + n\overline{I}_{L_2}$ and $\triangle i_{L_1} + n\triangle i_{L_2}$. $i_{L_1} + ni_{L_2}$ does not include the dc offset, so use of this current simplifies calculation of the inequality. If $\overline{I}_{L_1} + n\overline{I}_{L_2} \geq \triangle i_{L_1} + n\triangle i_{L_2}$, the Cuk inverter operates in CCM; otherwise, it operates in DCM.

By applying the current-second balance law to the capacitors C_1 and C_2, the relationship between average currents $\overline{I}_{L_1}$ and $\overline{I}_{L_2}$ can be expressed as

$$\frac{\overline{I}_{L_1}}{nD_{\text{CCM}}(t)} = \frac{\overline{I}_{L_2}}{1 - D_{\text{CCM}}(t)}. \tag{28}$$

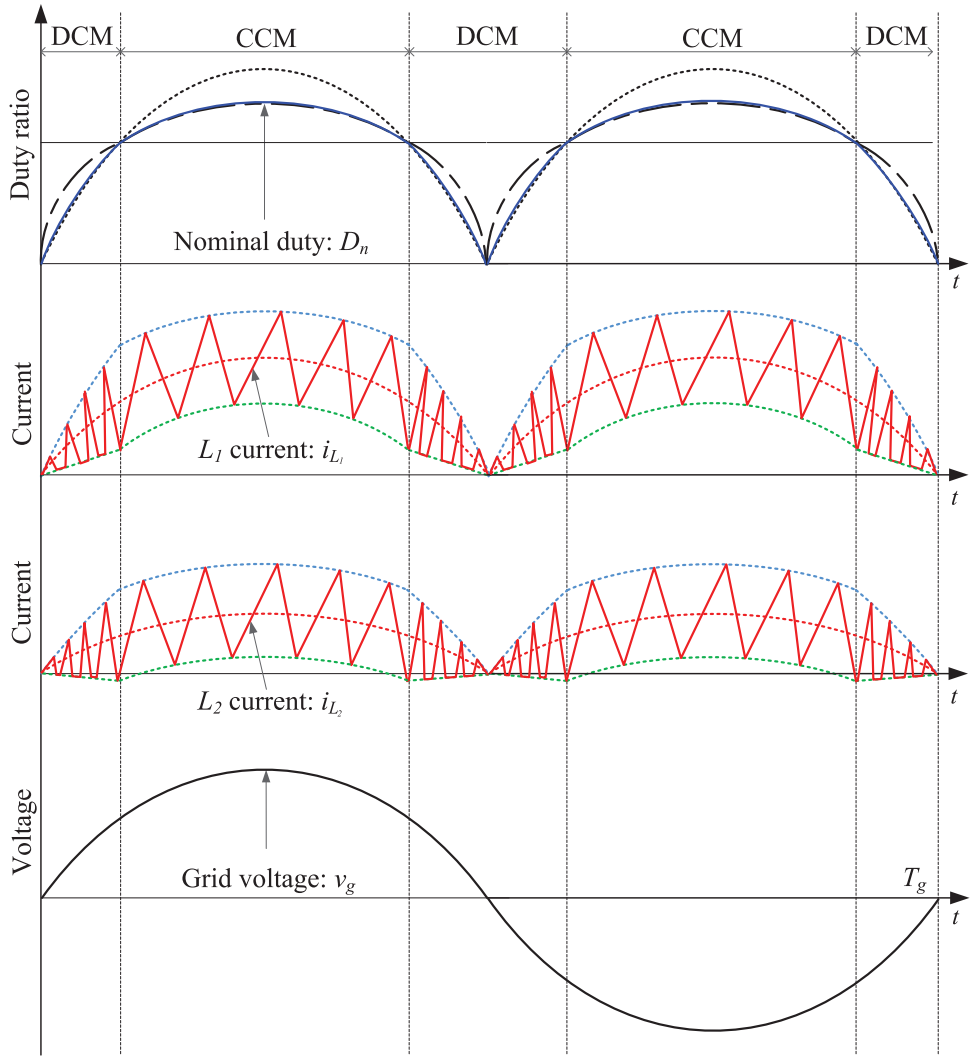

Fig. 4. Waveforms of the nominal duty ratio D_n, the current i_{L_1}, and the grid voltage v_g of the dual-mode Cuk inverter during the cycle of the grid period. Dotted black line: D_{DCM}; dashed black line: D_{CCM}; solid blue line: D_n; dotted blue line: outline of the peak current; dotted green line: outline of valley current; dotted red line: outline of average current; solid red line: instantaneous current i_{L_1}; solid black line: grid voltage; T_g: grid period.

From (18) and (19), the sum of current ripples is expressed as

$$\begin{aligned}\triangle i_{L_1} + n\triangle i_{L_2} &= V_{\mathrm{in}} T_s \left(\frac{1}{L_1} + \frac{n^2}{L_2}\right) D_{\mathrm{CCM}}(t) \\ &= \frac{V_{\mathrm{in}} T_s}{L_{\mathrm{eq}}} D_{\mathrm{CCM}}(t). \end{aligned} \tag{29}$$

If the inductor currents satisfy

$$\overline{I}_{L_1} + n\overline{I}_{L_2} \geq \frac{1}{2}(\triangle i_{L_1} + n\triangle i_{L_2}) \tag{30}$$

it operates in CCM; otherwise, it operates in DCM. Substituting (28) and (29) into (30) yields

$$\frac{n\overline{I}_{l_2}}{1 - D_{\mathrm{CCM}}(t)} \geq \frac{V_{\mathrm{in}} T_s}{2L_{\mathrm{eq}}} D_{\mathrm{CCM}}(t). \tag{31}$$

Substituting (27) into the left-hand side of (31) and rearranging it yields

$$\frac{|V_g| \cdot \overline{I}_{l_2}}{V_{\mathrm{in}}} \geq \frac{V_{\mathrm{in}} T_s}{2L_{\mathrm{eq}}} D^2_{\mathrm{CCM}}(t). \tag{32}$$

Applying the current-second balance law to the capacitor C_3 yields $\overline{I}_{L_2} = |I_g|$; substituting this equation into (32) yields

$$\frac{2L_{\mathrm{eq}}|V_g| \cdot |I_g|}{V^2_{\mathrm{in}} T_s} \geq D^2_{\mathrm{CCM}}(t). \tag{33}$$

Using $|V_g||I_g| = 2P_o \sin^2 \omega t$ and taking the square root on both sides of (33) yields

$$\frac{2}{V_{\mathrm{in}}} \sqrt{\frac{L_{\mathrm{eq}} P_o}{T_s}} |\sin \omega t| = D_{\mathrm{DCM}}(t) \geq D_{\mathrm{CCM}}(t). \tag{34}$$

As a result, if $D_{\mathrm{DCM}}(t) \geq D_{\mathrm{CCM}}(t)$, the converter operates in CCM; otherwise, it operates in DCM. The resulting nominal

TABLE I
PARAMETERS AND COMPONENTS OF THE PROTOTYPE DUAL-MODE CUK INVERTER

Parameters	Symbols	Values
Input voltage	V_i	60 V_{dc}
Grid voltage	v_g	220 V_{rms}
Rated output power	P_o	500 W
Grid frequency	f_g	60 Hz
Transformer turns ratio	$N_p : N_s$	11:31
Switching frequency	f_s	40 kHz
First capacitance	C_1	4.4 μF
Second capacitance	C_2	100 nF
Third capacitance	C_3	470 nF
First inductance	L_1	360 μH
Second inductance	L_2	570 μH
Filter inductance	L_f	300 μH
Components	Symbols	Part numbers
Switch	S_1	IPP200N25N3G
Transformer core	T	PQ3535
Diode	D_1	C2D05120A
Unfolding bridge switch	$S_2 - S_5$	IPP60R074C6

duty ratio D_n for the dual-mode Cuk inverter is obtained as

$$D_n(t) = \begin{cases} D_{\text{DCM}}(t), & \text{if} \quad D_{\text{DCM}}(t) < D_{\text{CCM}}(t) \\ D_{\text{CCM}}(t), & \text{if} \quad D_{\text{DCM}}(t) \geq D_{\text{CCM}}(t). \end{cases} \tag{35}$$

Although the nominal duty ratio D_n does not directly determine the output current, the use of dual-mode nominal duty ratio as the feedforward control input helps the dual-mode Cuk inverter to generate the desired output current by alleviating the effect of disturbances. Thus, the use of the dual-mode nominal duty ratio reduces the burden of the feedback controller, and thereby improving the overall control system performance.

In addition, we obtained the critical duty ratio value D_{crit} when $D_{\text{DCM}}(t) = D_{\text{CCM}}(t)$. Substituting the nominal duty ratios in DCM and CCM into $D_{\text{DCM}}(t) = D_{\text{CCM}}(t)$ yields

$$\frac{2}{V_{\text{in}}}\sqrt{\frac{L_{\text{eq}}P_o}{T_s}}|\sin\omega t| = \frac{|V_g|}{nV_{\text{in}} + |V_g|}. \tag{36}$$

Substituting $|V_g| = \sqrt{2}V_{\text{rms}}|\sin\omega t|$ into (36) and dividing both sides by $|\sin\omega t|$ yields

$$\frac{2}{V_{\text{in}}}\sqrt{\frac{L_{\text{eq}}P_o}{T_s}} = \frac{\sqrt{2}V_{\text{rms}}}{nV_{\text{in}} + \sqrt{2}V_{\text{rms}}|\sin\omega t|}. \tag{37}$$

Rearranging (37) to isolate $|\sin\omega t|$ yields

$$|\sin\omega t| = \frac{V_{\text{in}}}{2}\sqrt{\frac{T_s}{L_{\text{eq}}P_o}} - \frac{nV_{\text{in}}}{\sqrt{2}V_{\text{rms}}}. \tag{38}$$

Then, substituting (38) into (23) yields the critical duty ratio

$$D_{\text{crit}} = 1 - \frac{n}{V_{\text{rms}}}\sqrt{\frac{2L_{\text{eq}}P_o}{T_s}}. \tag{39}$$

From (39) and the conditions given in Table I, we can obtain the critical duty ratio of the dual-mode Cuk inverter according to the values of L_1 and L_2 [see Fig. 5(a)]. By multiplying $\sqrt{2}V_{\text{rms}}$ on both sides of (38), we can obtain the boundary of the operating modes with regard to $|V_g|$. Then, we also obtain the operating region and critical duty ratio according to the value of L_{eq} [see Fig. 5(b)]. As L_1 and L_2 decrease, the critical duty ratio increases. Appropriate values of L_1 and L_2 determines the critical duty ratio that results the balance of the operating regions between DCM and CCM.

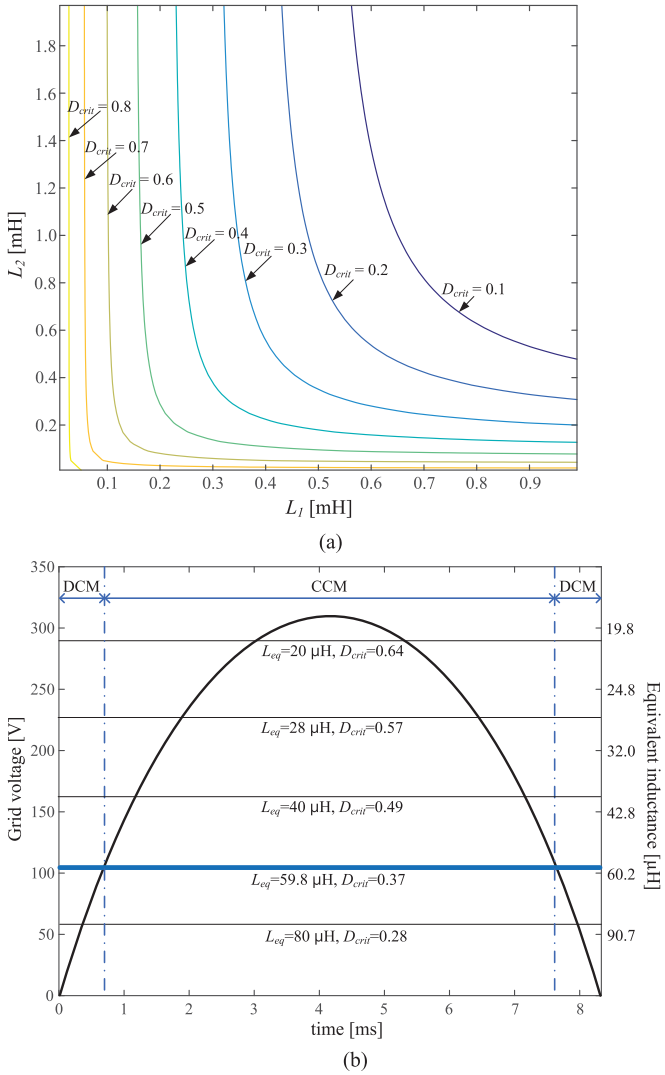

Fig. 5. Critical duty ratio and operating regions of dual-mode Cuk inverter. (a) Critical duty ratios according to the values of L_1 and L_2. (b) Operating region and critical duty ratio according to the value of L_{eq}.

C. Repetitive Controller With Multiple Phase-Lead Compensator and Stability Analysis

The RC is an effective solution to reject periodic errors in a dynamic system. The RC can provide an infinite gain for a specified frequency and its multiples and is often used to track a periodic signal and to suppress the disturbance of specified frequency components [31], [33]–[35]. However, if the RC is applied by itself to the dual-mode Cuk inverter, the different system dynamics in DCM and CCM may severely degrade the RC system performance. Thus, in the proposed RC, we mainly used the multiple phase-lead compensator to compensate for the phase lag of the dual-mode Cuk inverter.

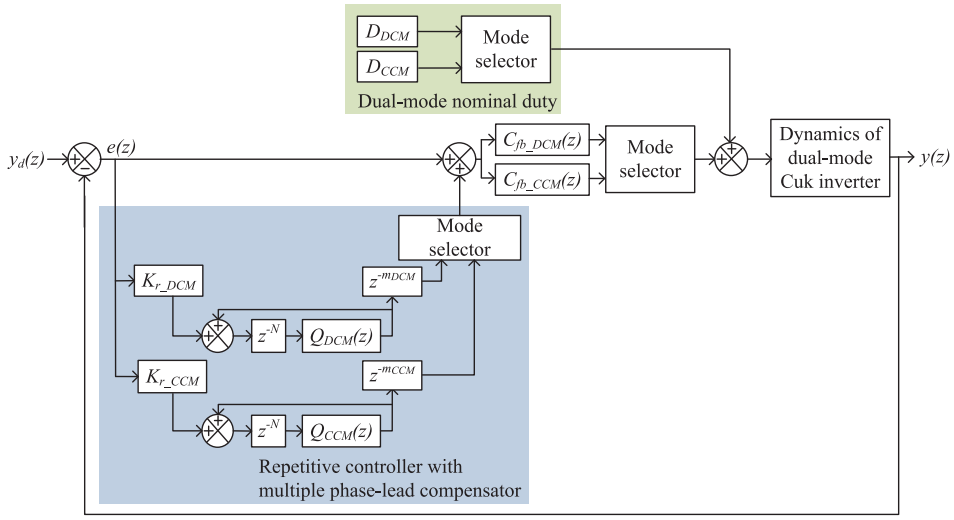

Fig. 6. Schematic diagram of control system for the dual-mode Cuk inverter. $y(z)$ and $y_d(z)$ are, respectively, the output and the reference output trajectories.

The proposed RC for the dual-mode Cuk inverter is described as follows:

$$C_{\text{rc\_DCM}}(z) = k_{r\_\text{DCM}} \frac{z^{-N} Q_{\text{DCM}}(z)}{1 - z^{-N} Q_{\text{DCM}}(z)} G_{\text{pl\_DCM}}(z) \tag{40}$$

$$C_{\text{rc\_CCM}}(z) = k_{r\_\text{CCM}} \frac{z^{-N} Q_{\text{CCM}}(z)}{1 - z^{-N} Q_{\text{CCM}}(z)} G_{\text{pl\_CCM}}(z) \tag{41}$$

where k_{r_DCM} and k_{r_CCM} are the RC gains in DCM and CCM; $N = f_s/f_g$ where $f_s = 1/T_s$ and f_g are, respectively, the switching and reference frequencies; $Q_{\text{DCM}}(z)$ and $Q_{\text{CCM}}(z)$ are the low-pass filters for the system robustness in DCM and CCM, respectively; and $G_{\text{pl\_DCM}}(z)$ and $G_{\text{pl\_CCM}}(z)$ are phase-lead compensators to compensate for the phase lag of the closed-loop systems in DCM and CCM, respectively. We select $G_{\text{pl\_DCM}}(z)$ and $G_{\text{pl\_CCM}}(z)$ as simple phase-lead compensators [39], [40]

$$G_{\text{pl\_DCM}}(z) = z^{m_{\text{DCM}}} \tag{42}$$

$$G_{\text{pl\_CCM}}(z) = z^{m_{\text{CCM}}} \tag{43}$$

where m_{DCM} and m_{CCM} are the prediction indexes in DCM and CCM, respectively.

The overall control system (see Fig. 6) consists of a PI controller term that forces the closed-loop system to stay within a uniform bound, a dual-mode nominal duty ratio term that roughly generates the desired output current, and an RC with multiple phase-lead compensator term that significantly improves the tracking accuracy.

To analyze the stability of the dual-mode Cuk inverter system, we use the small-signal model $G_{\text{id\_}\rho}(z)$ in (12) and (13). ρ is either DCM or CCM. From Fig. 6, we obtain

$$y(z) = e(z) \left(1 + k_{r\_\rho} \frac{Q_\rho(z) z^{-N}}{1 - Q_\rho(z) z^{-N}} z^{m_\rho}\right) \times C_{\text{fb\_}\rho}(z) G_{\text{id\_}\rho}(z) \tag{44}$$

$$e(z) = y_d(z) - y(z). \tag{45}$$

Substituting (44) into (45) yields

$$y_d(z) = e(z) \left(C_{\text{fb\_}\rho}(z) G_{\text{id\_}\rho}(z) + k_{r\_\rho} \frac{Q_\rho(z) z^{-N}}{1 - Q_\rho(z) z^{-N}} \cdot z^{m_\rho} C_{\text{fb\_}\rho}(z) G_{\text{id\_}\rho}(z) + 1\right). \tag{46}$$

$$\begin{aligned}
\frac{e(z)}{y_d(z)} &= \frac{1 - Q_\rho(z) z^{-N}}{C_{\text{fb_}\rho}(z) G_{\text{id_}\rho}(z)(1 - Q_\rho(z) z^{-N}) + k_{r_\rho} Q_\rho(z) \cdot z^{-N} z^{m_\rho} C_{\text{fb_}\rho}(z) G_{\text{id_}\rho}(z) + (1 - Q_\rho(z) z^{-N})} \\
&= \frac{1 - Q_\rho(z) z^{-N}}{(1 + C_{\text{fb_}\rho}(z) G_{\text{id_}\rho}(z))(1 - Q_\rho(z) z^{-N}) + k_{r_\rho} \cdot Q_\rho(z) z^{-N} z^{m_\rho} C_{\text{fb_}\rho}(z) G_{\text{id_}\rho}(z)} \\
&= \frac{(1 - Q_\rho(z) z^{-N}) \frac{1}{(1 + C_{\text{fb_}\rho}(z) G_{\text{id_}\rho}(z))}}{1 - Q_\rho(z) z^{-N} + k_{r_\rho} Q_\rho(z) z^{-N} z^{m_\rho} \cdot \frac{C_{\text{fb_}\rho}(z) G_{\text{id_}\rho}(z)}{(1 + C_{\text{fb_}\rho}(z) G_{\text{id_}\rho}(z))}} \\
&= \frac{(1 - Q_\rho(z) z^{-N})(1 - G_{\text{cl_}\rho}(z))}{1 - Q_\rho(z) z^{-N} + k_{r_\rho} Q_\rho(z) z^{-N} z^{m_\rho} G_{\text{cl_}\rho}(z)} \\
&= \frac{(1 - Q_\rho(z) z^{-N})(1 - G_{\text{cl_}\rho}(z))}{1 - Q_\rho(z) z^{-N}(1 - k_{r_\rho} z^{m_\rho} G_{\text{cl_}\rho}(z))}
\end{aligned} \tag{48}$$

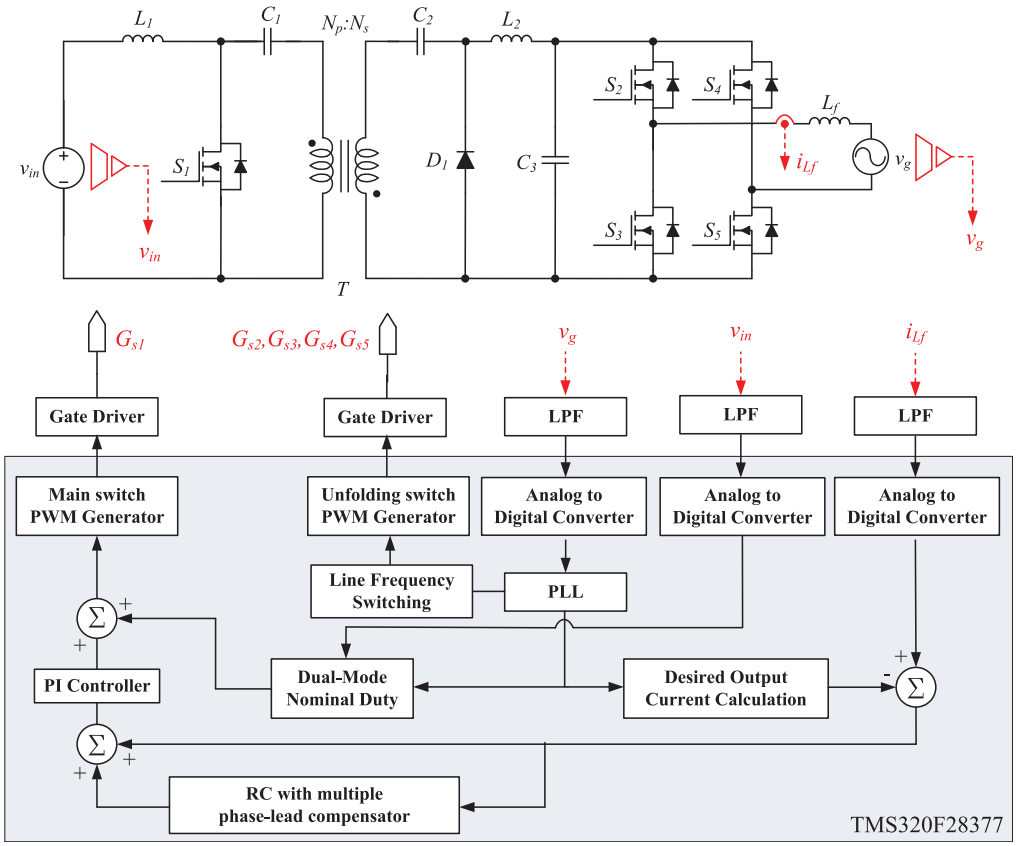

Fig. 7. Configuration of the proposed control system. LPF and PLL stand for low-pass filter and phase-locked loop.

Multiplying both sides of (46) by $1 - Q_\rho(z)z^{-N}$ yields

$$\begin{aligned} y_d(z)(1 - Q_\rho(z)z^{-N}) = e(z)(&C_{\text{fb\_}\rho}(z)G_{\text{id\_}\rho}(z) \\ &(1 - Q_\rho(z)z^{-N}) + k_{r\_\rho}Q_\rho(z) \\ &\cdot z^{-N}z^{m_\rho}C_{\text{fb\_}\rho}(z)G_{\text{id\_}\rho}(z) \\ &+ (1 - Q_\rho(z)z^{-N})). \end{aligned} \tag{47}$$

Rearranging (47) yields (48) shown at the bottom of the previous page, where $G_{\text{cl\_}\rho}(z) = C_{\text{fb\_}\rho}(z)G_{\text{id\_}\rho}(z)/(1 + C_{\text{fb\_}\rho}(z)G_{\text{id\_}\rho}(z))$ is the closed-loop transfer function without the RC in DCM and CCM.

The transfer function $e(z)/y_d(z)$ can be written as three terms connected in cascade. The term $1 - Q_\rho(z)z^{-N}$ has a low-pass filter and a time delay, which is stable. The term $1 - G_{\text{cl\_}\rho}(z)$ has the same roots as $G_{\text{cl\_}\rho}(z)$ and is stable if $G_{\text{cl\_}\rho}(z)$ is stable. Finally, the term $1/(1 - Q_\rho(z)z^{-N}[1 - k_{r\_\rho}z^{m_\rho}G_{\text{cl\_}\rho}(z)])$ can be described as a positive feedback closed-loop system with the term $Q_\rho(z)z^{-N}[1 - k_{r\_\rho}z^{m_\rho}G_{\text{cl\_}\rho}(z)]$ in the feedback path. According to the small-gain theorem, the stability of the term $1 - Q_\rho(z)z^{-N}[1 - k_{r\_\rho}z^{m_\rho}G_{\text{cl\_}\rho}(z)]$ is guaranteed whenever

$$\begin{aligned} &|Q_\rho(z)z^{-N}(1 - k_{r\_\rho}z^{m_\rho}G_{\text{cl\_}\rho}(z))| \\ &\le |z^{-N}| \cdot |Q_\rho(z)(1 - k_{r\_\rho}z^{m_\rho}G_{\text{cl\_}\rho}(z))| \\ &\le |Q_\rho(z)(1 - k_{r\_\rho}z^{m_\rho}G_{\text{cl\_}\rho}(z))| < 1 \\ &\quad \text{for all } z = e^{jwT_s}, \quad \text{where } 0 < w < \frac{\pi}{T_s}. \end{aligned} \tag{49}$$

A sufficient condition for (49) is given by

$$|Q_\rho(z)| \le 1, \quad \text{for all } z = e^{jwT_s}, \quad \text{where } 0 < w < \frac{\pi}{T_s} \tag{50}$$

$$\begin{aligned} &|1 - k_{r\_\rho}z^{m_\rho}G_{\text{cl\_}\rho}(z)| < 1 \\ &\quad \text{for all } z = e^{jwT_s}, \quad \text{where } 0 < w < \frac{\pi}{T_s}. \end{aligned} \tag{51}$$

Then, the overall control system will be stable whenever three stability conditions are satisfied, which are as follows.

a) The closed-loop system $G_{\text{cl\_}\rho}(z)$ without the RC is stable.
b) $|Q_\rho(z)| \le 1$, for all $z = e^{jwT_s}$, where $0 < w < \frac{\pi}{T_s}$.
c) $|1 - k_{r\_\rho}z^{m_\rho}G_{\text{cl\_}\rho}(z)| < 1$, for all $z = e^{jwT_s}$, where $0 < w < \frac{\pi}{T_s}$.

D. Design Guideline for the Proposed Controller

In this section, we introduce guidelines to design $C_{\text{fb\_}\rho}(z)$, $Q_\rho(z)$, z^{m_ρ}, and k_{r_ρ} such that they satisfy the stability conditions listed in Section III-C. Stability condition (a) means that $C_{\text{fb\_}\rho}(z)$ must be designed to be stable even without the RC. This condition is satisfied whenever $1 + C_{\text{fb\_}\rho}(z)G_{\text{id\_}\rho}(z)$ has no roots outside the unit circle in the z-plane. $Q_\rho(z)$ satisfies stability condition (b) if we design $Q_\rho(z)$ as a moving average filter with zero phase shift

$$Q_\rho(z) = \Sigma_{i=0}^{p}\alpha_{i\_\rho}z^{i} + \Sigma_{i=1}^{p}\alpha_{i\_\rho}z^{-i} \tag{52}$$

where $\alpha_{0\_\rho} + 2\Sigma_{i=1}^{p}\alpha_{i\_\rho} = 1$ with $\alpha_{i\_\rho} > 0$ and p is the number

of samples to be used for filtering.

Using the frequency-domain design approach [38]–[40], $G_{\mathrm{cl}\_\rho}(z)$ can be described as $G_{\mathrm{cl}\_\rho}(e^{j\omega T_s}) = N_{g\_\rho}(e^{j\omega T_s})\exp(j\theta_{g\_\rho}(e^{j\omega T_s}))$, where $N_{g\_\rho}(e^{j\omega T_s}) = |G_{\mathrm{cl}\_\rho}(e^{j\omega T_s})|$ and $\theta_{g\_\rho}(e^{j\omega T_s}) = \angle G_{\mathrm{cl}\_\rho}(e^{j\omega T_s})$. The phase-lead compensator z^{m_ρ} can be represented as $z^{m_\rho} = \exp(j\theta_{m_\rho}(e^{j\omega T_s}))$. Substituting $G_{\mathrm{cl}\_\rho}(e^{j\omega T_s}) = N_{g\_\rho}(e^{j\omega T_s})\exp(j\theta_{g\_\rho}(e^{j\omega T_s}))$ and $z^{m_\rho} = \exp(j\theta_{m_\rho}(e^{j\omega T_s}))$ into stability condition (c) yields

$$\left|1 - k_{r\_\rho}N_{g\_\rho}(e^{j\omega T_s})e^{j(\theta_{g\_\rho}(e^{j\omega T_s})+\theta_{m_\rho}(e^{j\omega T_s}))}\right| < 1. \tag{53}$$

Because $e^{j\theta} = \cos(\theta) + j\sin(\theta)$ and $k_{r\_\rho} > 0$, (53) can be simplified to

$$\begin{aligned} &- 2k_{r\_\rho}N_{g\_\rho}(e^{j\omega T_s})\cos(\theta_{g\_\rho}(e^{j\omega T_s}) + \theta_{m_\rho}(e^{j\omega T_s})) \\ &+ k_{r\_\rho}^2 N_{g\_\rho}^2(e^{j\omega T_s}) < 0. \end{aligned} \tag{54}$$

Sufficient conditions for (54) are

$$0 < k_{r\_\rho} < \frac{2\cos(\theta_{g\_\rho}(e^{j\omega T_s}) + \theta_{m_\rho}(e^{j\omega T_s}))}{N_{g\_\rho}(e^{j\omega T_s})} \tag{55}$$

and

$$|\theta_{g\_\rho}(e^{j\omega T_s}) + \theta_{m_\rho}(e^{j\omega T_s})| < \pi/2. \tag{56}$$

By choosing an appropriate phase-lead step m_ρ, the frequency band of (56) will increase and the number of error harmonic components that can be eliminated will increase. Moreover, the range from which k_{r_ρ} can be selected will also increase.

IV. Experiment

A 500-W experimental dual-mode Cuk inverter was constructed to demonstrate the feasibility of the proposed controller. The experiment was performed using a prototype of the dual-mode Cuk inverter with circuit parameters and operating conditions (see Table I and Fig. 7). The control algorithms were implemented using a TMS320F28377 microcontroller.

Based on the fifth-order model (12), (13), we designed the proposed RC for the developed Cuk inverter. Operating points in DCM and CCM are, respectively, set at the instantaneous output power 80 W and the instantaneous peak output power of 500 W with full load. At these points, the transfer functions of the dual-mode Cuk inverter are DCM

$$G_{\mathrm{id\_DCM}}(z) = \frac{-27.97z^5 + 30.46z^4 + 21.11z^3 - 0.004z^2}{-16.32z^5 - 32.52z^4 + 22.92z^3 - 12.39z^2 + 1.26z - 0.07}. \tag{57}$$

CCM

$$G_{\mathrm{id\_CCM}}(z) = \frac{-68.33z^5 + 54.65z^4 + 19.73z^3 - 0.004z^2}{22.75z^5 - 39.82z^4 + 27.99z^3 - 13.30z^2 + 2.98z - 0.59}. \tag{58}$$

The PI controllers in DCM and CCM were designed to satisfy stability condition (a); we simply set the gains of the PI

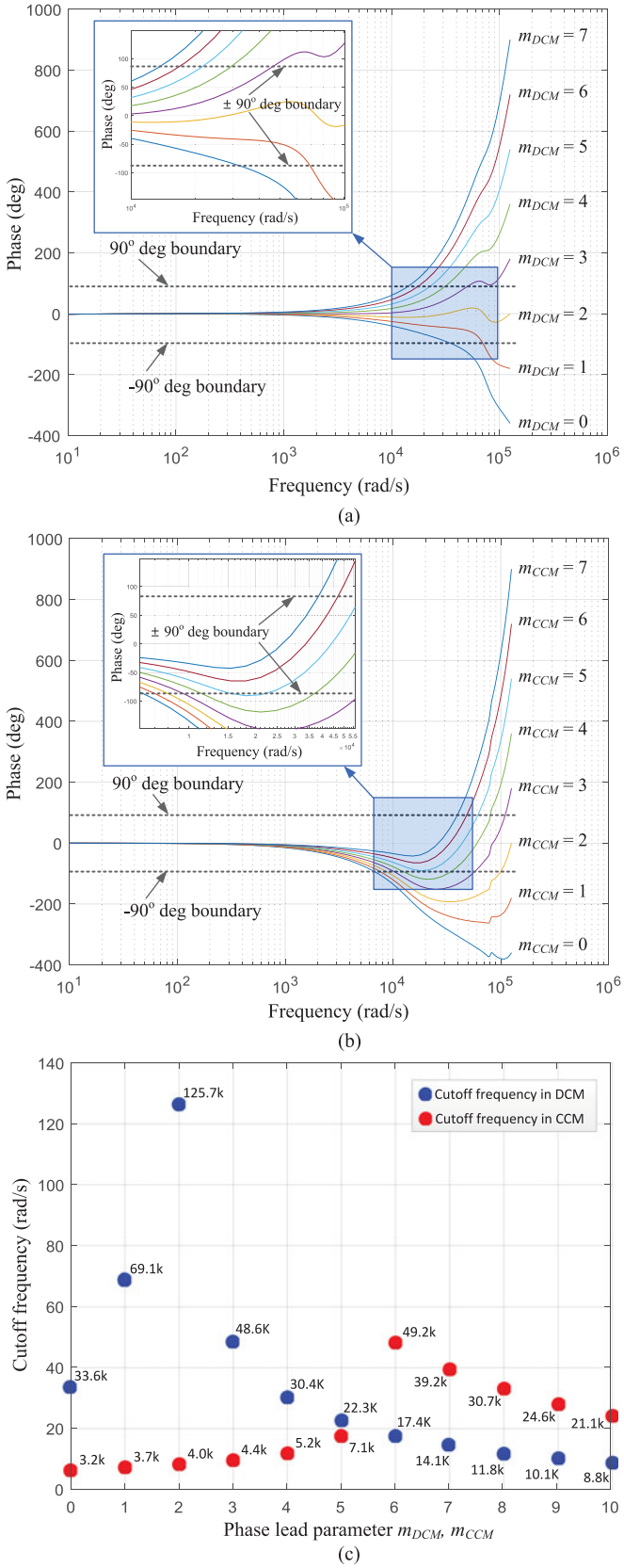

Fig. 8. Phase plots of the closed-loop feedback system with different phase-lead steps. (a) In DCM. (b) In CCM. (c) Cutoff frequencies versus m in DCM (blue) and CCM (red).

TABLE II
RANGES OF k_{r_ρ} OVER WHICH THE DUAL-MODE CUK INVERTER IS STABLE AT DIFFERENT VALUES OF m_{DCM} AND m_{CCM}

$m_{\mathrm{DCM}}/m_{\mathrm{CCM}}$	0, 1	2,...5	6, 7	8, 9	10
0	Unstable	Unstable	Unstable	Unstable	Unstable
1	Unstable	$k_{r\_\rho} = 0.01$	$0.01 \le k_{r\_\rho} \le 0.03$	$k_{r\_\rho} = 0.01$	Unstable
2, 3	Unstable	$0.01 \le k_{r\_\rho} \le 0.02$	$0.01 \le k_{r\_\rho} \le 0.04$	$0.01 \le k_{r\_\rho} \le 0.02$	Unstable
4,...,7	Unstable	Unstable	$0.01 \le k_{r\_\rho} \le 0.02$	$k_{r\_\rho} = 0.01$	Unstable
8,...,10	Unstable	Unstable	Unstable	Unstable	Unstable

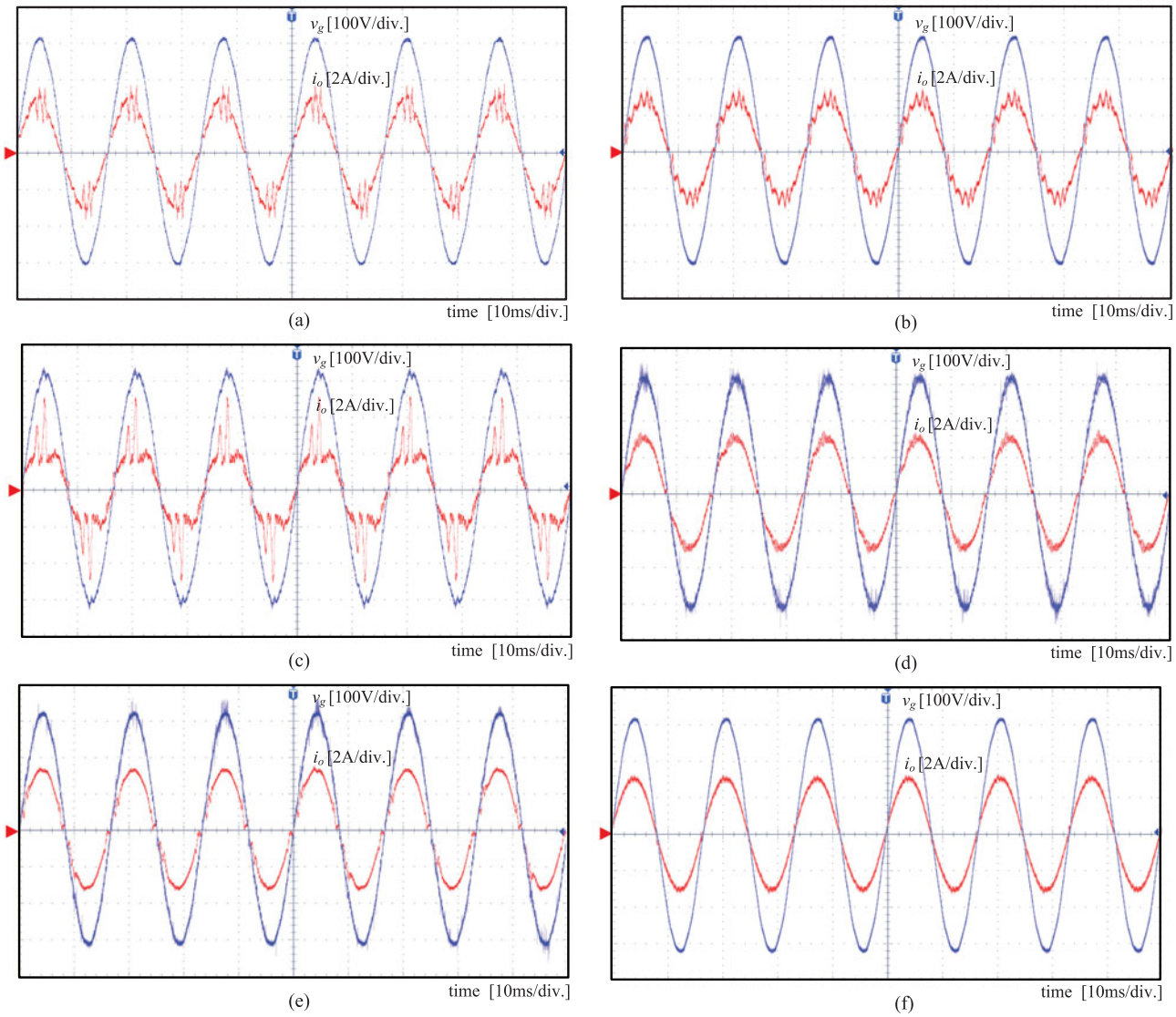

Fig. 9. Experimental waveforms of the grid voltage and output current at output power $P_o = 500$ W. (a) PI controller is used. (b) Proportional-resonant (PR) controller is used. (c) RC without phase-lead step. (d) RC with phase-lead step $m_{\mathrm{DCM}} = m_{\mathrm{CCM}} = 2$. (e) RC with phase-lead step $m_{\mathrm{DCM}} = m_{\mathrm{CCM}} = 6$. (f) RC with phase-lead steps $m_{\mathrm{DCM}} = 2$ and $m_{\mathrm{CCM}} = 6$.

controllers as $k_{p\_\mathrm{DCM}} = k_{p\_\mathrm{CCM}} = 0.1$ and $k_{i\_\mathrm{DCM}} = k_{i\_\mathrm{CCM}} = 0.9$. The poles of the closed-loop systems in DCM and CCM are located in the unit circle of the z-plane, so the closed-loop systems without the RC are stable.

The low-pass filters $Q_{\mathrm{DCM}}(z)$ and $Q_{\mathrm{CCM}}(z)$ were designed as $0.25z + 0.5 + 0.25z^{-1}$, which naturally meets stability condition (b). The phase-lead steps m_{DCM} and m_{CCM} and the RC gains k_{r_DCM} and k_{r_CCM} must be selected to satisfy stability condition (c) in both DCM and CCM.

The phase of the closed-loop feedback system in DCM without RC and with $m_{\mathrm{DCM}} = 0$ rapidly decreases below -90° due to the phase lag caused by the two RHP zeros [see Fig. 8(a)]. Likewise, the phase of the closed-loop feedback system in CCM without RC and with $m_{\mathrm{CCM}} = 0$ also decreases below

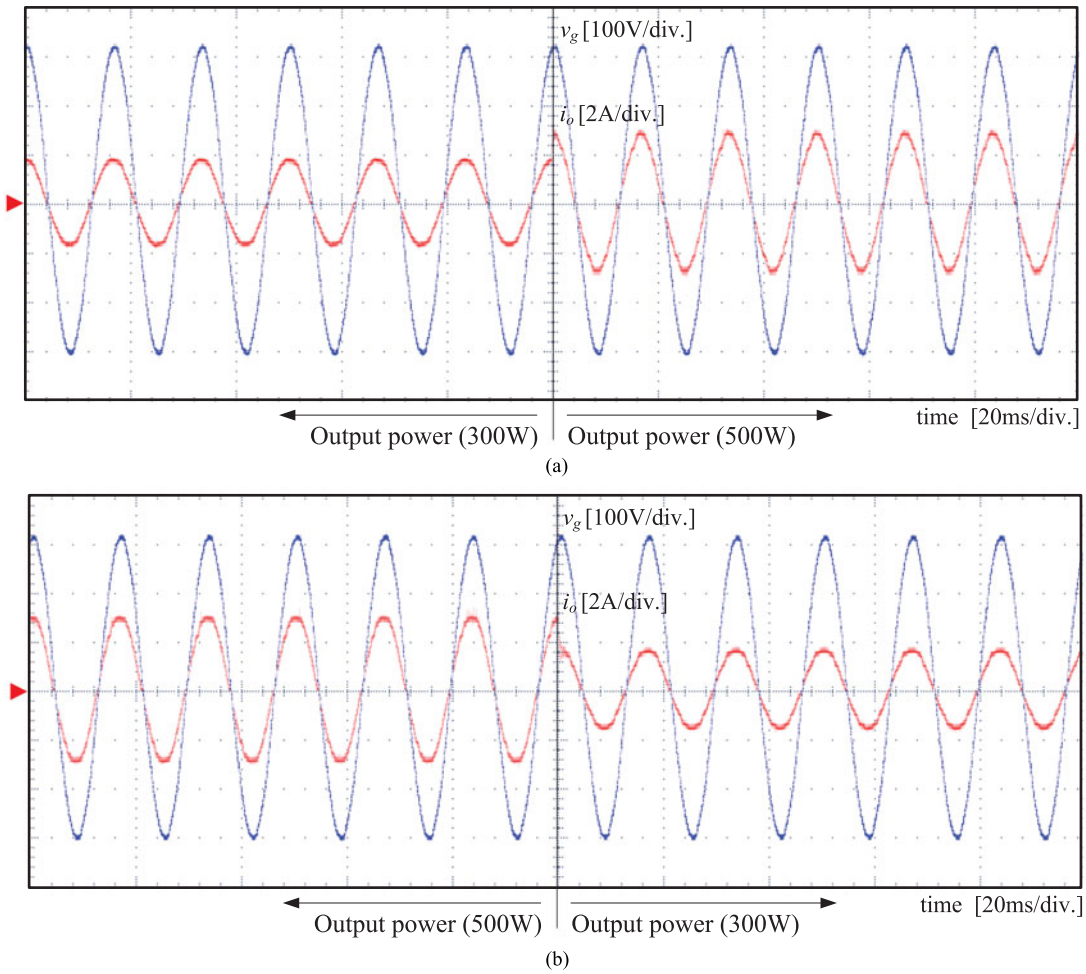

Fig. 10. Experimental waveforms of the grid voltage and output current when the output power is (a) step-up from 300 to 500 W and (b) step-down from 500 to 300 W.

-90° due to the phase lag caused by the two RHP zeros [see Fig. 8(b)]; therefore, $m_{\rm DCM}$ and $m_{\rm CCM}$ must be selected to compensate for the phase lag of the closed-loop system in DCM and CCM, respectively. When we set $m_{\rm DCM} = 2$ and $m_{\rm CCM} = 6$, the closed-loop systems in DCM and CCM achieved relatively wide frequency bandwidth [see Fig. 8(a) and (b)]. Based on these $m_{\rm DCM}$ and $m_{\rm CCM}$, we must select the corresponding RC gains $0 \le k_{r\_{\rm DCM}} \le 3.455$ and $0 \le k_{r\_{\rm CCM}} \le 0.177$. The low-pass filter attenuates the magnitude of the closed-loop systems at high frequencies, so the large phase shift at high frequencies has no effect on the system stability.

Theoretical analysis of the phase-lead compensator indicates that $m_{\rm DCM} = 2$ and $m_{\rm CCM} = 6$ are the optimal number of lead steps for the RC. In practice, due to unknown uncertainties and various grid disturbances, $m_{\rm DCM} = 2$ and $m_{\rm CCM} = 6$ do not sufficiently compensate for phase lag in closed-loop systems. The optimal $m_{\rm DCM}$ and $m_{\rm CCM}$ can be determined by experimentation. Experiments with the RC gains $k_r = 0.01, \ldots, 0.04$ and different values of $m_{\rm DCM}$ and $m_{\rm CCM}$ yielded the stability results of the corresponding closed-loop systems (see Table II). From Fig. 8 and Table II, the closed-loop feedback systems $G_{\rm id\_DCM}$ and $G_{\rm id\_CCM}$ with the rated power 500 W were stable when $1 \le m_{\rm DCM} \le 3$ and $6 \le m_{\rm CCM} \le 7$. In our experiment, we set phase-lead $m_{\rm DCM} = 2$ and $m_{\rm CCM} = 6$ and RC gain $k_{r\_{\rm DCM}} = k_{r\_{\rm CCM}} = 0.01$.

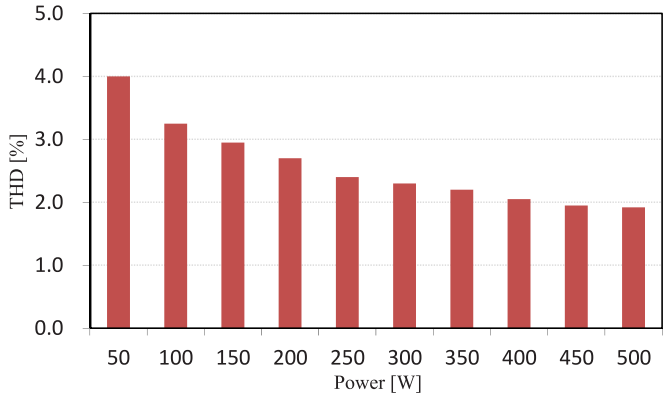

Fig. 11. THD on the output current.

We first describe the difficulty in controlling the output current of the dual-mode Cuk inverter when the conventional controller or the RC with inappropriate phase-lead compensator are used (see Fig. 9). When the conventional PI plus the feedforward

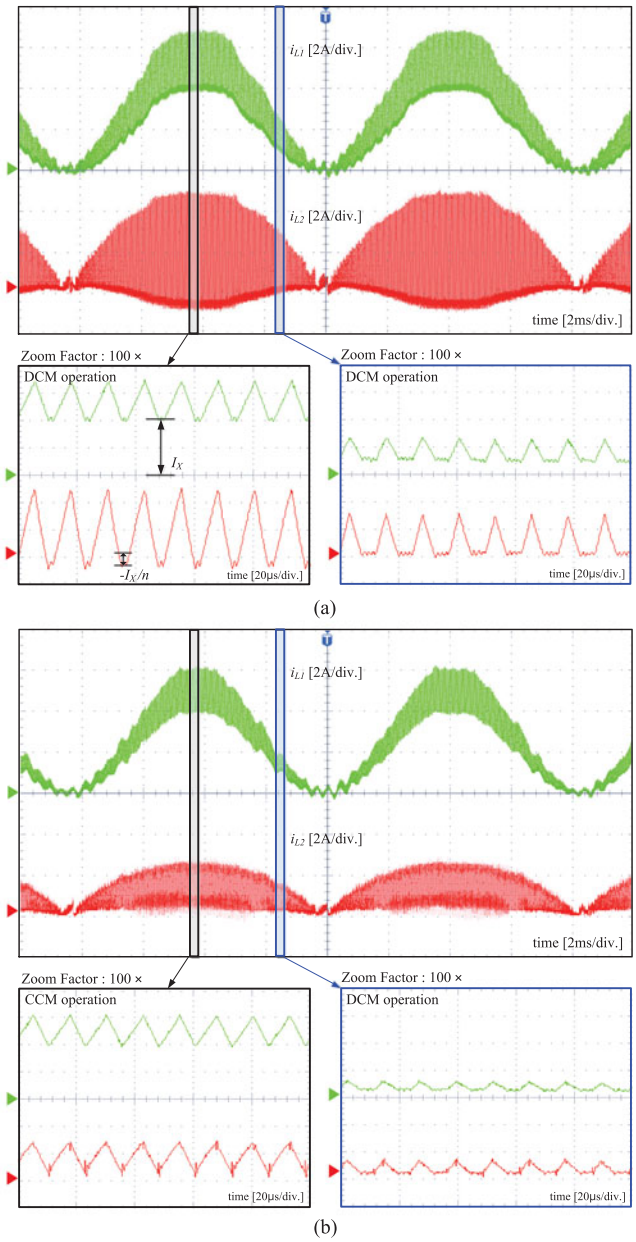

Fig. 12. Experimental waveforms of current i_{L_1} and i_{L_2} at output power P_o = 250 W. (a) In DCM. (b) In dual-mode.

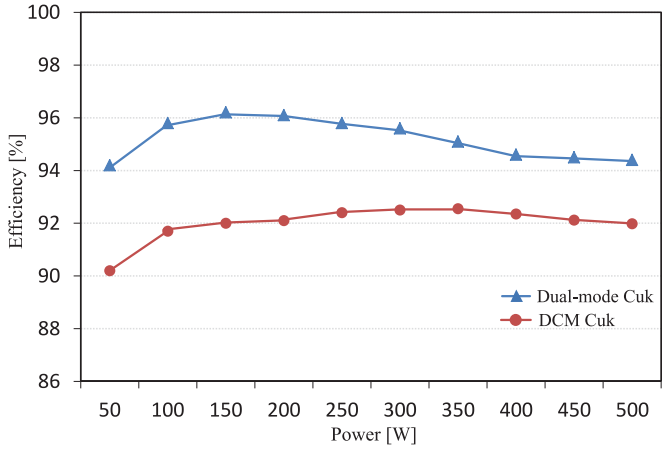

Fig. 13. Measured power conversion efficiency under different load conditions.

controller was used, the output current was highly fluctuated [see Fig. 9(a)] as a result from both the effect of two RHP zeros and the grid voltage disturbance. When the PR controller is used, the output current was still distorted [see Fig. 9(b)]. This distortion stems from the fact that PR controller cannot compensate the phase lag caused by the two RHP zeros. When the RC without the phase-lead compensator was applied, the output current is still severely distorted [see Fig. 9(c)]. When the RC with two-step phase-lead was applied, the output current started to fluctuate in CCM due to the incorrect input learning [see Fig. 9(d)]. When the RC with six-step phase-lead was applied, the output current also started to oscillate in the DCM region [see Fig. 9(e)]. But when the proposed RC with two-step phase-lead in DCM region and six-step phase-lead in CCM region was used, the output current was almost sinusoidal and the dual-mode Cuk inverter achieved desired power level at 500 W [see Fig. 9(f)].

To verify the performance of the proposed controller during the load transition, we varied the output power from 300 to 500 W and vice versa (see Fig. 10). When the output power was changed, the output current was slightly distorted, but the actual output current tracked the reference output current well after in a few iterations. Total harmonic distortion (THD) of the output current was $\leq$1.92 % at the full-load condition (see Fig. 11).

Current stress was measured in the Cuk DCM inverter [see Fig. 12(a)] and the dual-mode Cuk inverter [see Fig. 12(b)]. To ensure DCM operation at all operating points, L_1 and L_2 of the Cuk DCM inverter were set to 110 μH and 180 μH, respectively, which can be obtained from (39) and Fig. 5. Current stresses were much lower on both inductors of primary and secondary sides in the dual-mode Cuk inverter than in the Cuk DCM inverter. Over the entire range of tested load condition, the dual-mode Cuk inverter achieved higher efficiency (maximum 96.15%) than the Cuk DCM inverter (see Fig. 13). Efficiency was measured using a digital power meter (Yokogawa WT130).

V. Conclusion

This paper has presented dynamic modeling of a dual-mode Cuk inverter and approaches to control it. We first derived the small-signal model of the dual-mode Cuk inverter; in this model, each transfer function of the operation mode has a distinct set of RHP zeros. We obtained the nominal duty ratio in each operation mode and the boundary between two operation modes. The dual-mode nominal duty ratio was used as the feedforward control input and supplemented with the conventional controller and the RC. To compensate for the different phase lags caused by the different system dynamics in DCM and CCM, we implemented an RC with a multiple phase-lead compensation algorithm in the proposed repetitive control scheme. We also provided detailed and practical design guidelines of the control parameters to develop a stable Cuk DCM/CCM inverter. Experimental results

using a 500-W prototype demonstrate that the proposed control scheme achieves the desired tracking performance.

APPENDIX A

The average model (4) can be described by the nonlinear differential equation $\dot{\mathbf{x}}(t) = \mathbf{F}(\mathbf{x}(t), d_1(t))$, where $\mathbf{F} = [F_1, F_2, \ldots, F_5]^T$ is a nonlinear functions and $\mathbf{x} = [x_1, x_2, x_3, x_4, x_5]^T$ is the state vector. Linearizing (4) yields the small-signal model in (6). The parameters used in (6) are given as follows:

$$\frac{\partial F_1}{\partial \hat{x}_1} = \frac{\partial A}{\partial \hat{x}_1}\left(\frac{R_{C_3} I_{L_1}}{n^2 L_{12}} - \frac{V_{C_{12}}}{nL_1} + \frac{V_{C_{12}}}{L_{12}} - \frac{V_{C_3}}{nL_{12}} + \frac{R_{C_3} I_{L_f}}{nL_{12}}\right) - \frac{R_{C_3}(1-A)}{n^2 L_{12}} \tag{59}$$

$$\frac{\partial F_1}{\partial \hat{x}_2} = \frac{\partial A}{\partial \hat{x}_2}\left(\frac{R_{C_3} I_{L_1}}{n^2 L_{12}} - \frac{V_{C_{12}}}{nL_1} + \frac{V_{C_{12}}}{L_{12}} - \frac{V_{C_3}}{nL_{12}} + \frac{R_{C_3} I_{L_f}}{nL_{12}}\right) \tag{60}$$

$$\frac{\partial F_1}{\partial \hat{x}_3} = \frac{\partial A}{\partial \hat{x}_3}\left(\frac{R_{C_3} I_{L_1}}{n^2 L_{12}} - \frac{V_{C_{12}}}{nL_1} + \frac{V_{C_{12}}}{L_{12}} - \frac{V_{C_3}}{nL_{12}} + \frac{R_{C_3} I_{L_f}}{nL_{12}}\right) - \left(\frac{A-D}{nL_1} + \frac{1-A}{L_{12}}\right) \tag{61}$$

$$\frac{\partial F_1}{\partial \hat{x}_4} = \frac{\partial A}{\partial \hat{x}_4}\left(\frac{R_{C_3} I_{L_1}}{n^2 L_{12}} - \frac{V_{C_{12}}}{nL_1} + \frac{V_{C_{12}}}{L_{12}} - \frac{V_{C_3}}{nL_{12}} + \frac{R_{C_3} I_{L_f}}{nL_{12}}\right) + \frac{1-A}{nL_{12}} \tag{62}$$

$$\frac{\partial F_1}{\partial \hat{x}_5} = \frac{\partial A}{\partial \hat{x}_5}\left(\frac{R_{C_3} I_{L_1}}{n^2 L_{12}} - \frac{V_{C_{12}}}{nL_1} + \frac{V_{C_{12}}}{L_{12}} - \frac{V_{C_3}}{nL_{12}} + \frac{R_{C_3} I_{L_f}}{nL_{12}}\right) - \frac{R_{C_3}(1-A)}{nL_{12}} \tag{63}$$

$$\frac{\partial F_1}{\partial \hat{d}} = \frac{\partial A}{\partial \hat{d}}\left(\frac{R_{C_3} I_{L_1}}{n^2 L_{12}} - \frac{V_{C_{12}}}{nL_1} + \frac{V_{C_{12}}}{L_{12}} - \frac{V_{C_3}}{nL_{12}} + \frac{R_{C_3} I_{L_f}}{nL_{12}}\right) + \frac{V_{C_{12}}}{nL_1} \tag{64}$$

$$\frac{\partial F_2}{\partial \hat{x}_1} = -\frac{\partial A}{\partial \hat{x}_1}\left(\frac{R_{C_3} I_{L_2}}{L_2} - \frac{R_{C_3} I_{L_2}}{n^2 L_{12}} + \frac{V_{C_{12}}}{n^2 L_{12}} + \frac{V_{C_3}}{L_2} - \frac{V_{C_3}}{n^2 L_{12}} - \frac{R_{C_3} I_{L_f}}{L_2} + \frac{R_{C_3} I_{L_f}}{n^2 L_{12}}\right) \tag{65}$$

$$\frac{\partial F_2}{\partial \hat{x}_2} = -\frac{\partial A}{\partial \hat{x}_2}\left(\frac{R_{C_3} I_{L_2}}{L_2} - \frac{R_{C_3} I_{L_2}}{n^2 L_{12}} + \frac{V_{C_{12}}}{n^2 L_{12}} + \frac{V_{C_3}}{L_2} - \frac{V_{C_3}}{n^2 L_{12}} + \frac{R_{C_3} I_{L_f}}{L_2} - \frac{R_{C_3} I_{L_f}}{n^2 L_{12}}\right) - \left(\frac{R_{C_3} A}{L_2} + \frac{R_{C_3}(1-A)}{n^2 L_{12}}\right) \tag{66}$$

$$\frac{\partial F_2}{\partial \hat{x}_3} = -\frac{\partial A}{\partial \hat{x}_3}\left(\frac{R_{C_3} I_{L_2}}{L_2} - \frac{R_{C_3} I_{L_2}}{n^2 L_{12}} + \frac{V_{C_{12}}}{n^2 L_{12}} + \frac{V_{C_3}}{L_2} - \frac{V_{C_3}}{n^2 L_{12}} - \frac{R_{C_3} I_{L_f}}{L_2} + \frac{R_{C_3} I_{L_f}}{n^2 L_{12}}\right) + \left(\frac{D}{L_2} + \frac{1-A}{n^2 L_{12}}\right) \tag{67}$$

$$\frac{\partial F_2}{\partial \hat{x}_4} = -\frac{\partial A}{\partial \hat{x}_4}\left(\frac{R_{C_3} I_{L_2}}{L_2} - \frac{R_{C_3} I_{L_2}}{n^2 L_{12}} + \frac{V_{C_{12}}}{n^2 L_{12}} + \frac{V_{C_3}}{L_2} - \frac{V_{C_3}}{n^2 L_{12}} - \frac{R_{C_3} I_{L_f}}{L_2} + \frac{R_{C_3} I_{L_f}}{n^2 L_{12}}\right) - \left(\frac{A}{L_2} + \frac{1-A}{n^2 L_{12}}\right) \tag{68}$$

$$\frac{\partial F_2}{\partial \hat{x}_5} = -\frac{\partial A}{\partial \hat{x}_5}\left(\frac{R_{C_3} I_{L_2}}{L_2} - \frac{R_{C_3} I_{L_2}}{n^2 L_{12}} + \frac{V_{C_{12}}}{n^2 L_{12}} + \frac{V_{C_3}}{L_2} - \frac{V_{C_3}}{n^2 L_{12}} - \frac{R_{C_3} I_{L_f}}{L_2} + \frac{R_{C_3} I_{L_f}}{n^2 L_{12}}\right) + \left(\frac{R_{C_3} A}{L_2} + \frac{R_{C_3}(1-A)}{n^2 L_{12}}\right) \tag{69}$$

$$\frac{\partial F_2}{\partial \hat{d}} = -\frac{\partial A}{\partial \hat{d}}\left(\frac{R_{C_3} I_{L_2}}{L_2} - \frac{R_{C_3} I_{L_2}}{n^2 L_{12}} + \frac{V_{C_{12}}}{n^2 L_{12}} + \frac{V_{C_3}}{L_2} - \frac{V_{C_3}}{n^2 L_{12}} - \frac{R_{C_3} I_{L_f}}{L_2} + \frac{R_{C_3} I_{L_f}}{n^2 L_{12}}\right) + \frac{V_{C_{12}}}{L_2} \tag{70}$$

where

$$A = \frac{2(I_{L_1} + nI_{L_2})L_1 L_2}{DT_s(L_2 V_{\text{in}} + L_1 n(V_{C_{12}} - V_{C_3})} \tag{71}$$

$$\frac{\partial A}{\partial \hat{x}_1} = \frac{2L_1 L_2}{DT_s(L_2 V_{\text{in}} + L_1 n(V_{C_{12}} - V_{C_3})} \tag{72}$$

$$\frac{\partial A}{\partial \hat{x}_2} = \frac{2nL_1 L_2}{DT_s(L_2 V_{\text{in}} + L_1 n(V_{C_{12}} - V_{C_3})} \tag{73}$$

$$\frac{\partial A}{\partial \hat{x}_3} = \frac{-2(I_{L_1} + nI_{L_2})L_1^2 L_2 n}{DT_s(L_2 V_{\text{in}}(t) + L_1 n(V_{C_{12}} - V_{C_3})^2} \tag{74}$$

$$\frac{\partial A}{\partial \hat{x}_4} = \frac{2(I_{L_1} + nI_{L_2})L_1^2 L_2 n}{DT_s(L_2 V_{\text{in}} + L_1 n(V_{C_{12}} - V_{C_3})^2} \tag{75}$$

$$\frac{\partial A}{\partial \hat{x}_5} = 0 \tag{76}$$

$$\frac{\partial A}{\partial \hat{d}} = \frac{-2(I_{L_1} + nI_{L_2})L_1 L_2}{D^2 T_s(L_2 V_{\text{in}} + L_1 n(V_{C_{12}} - V_{C_3})}. \tag{77}$$

APPENDIX B

The system parameters as defined in (10) and (11) are given as follows:

$$a_1 = -n^2 C_3 C_{12} R_{C_3} \frac{\partial G_2}{\partial \hat{d}} \tag{78}$$

$$a_2 = C_3 R_{C_3}(I_{L_1} + n^2 I_{L_2})\frac{\partial F_2}{\partial \hat{x}_3} - n^2 C_{12}\frac{\partial F_2}{\partial \hat{d}} + n^2 C_3 C_{12} R_{C_3}\left(\frac{\partial F_1}{\partial \hat{x}_1}\frac{\partial F_2}{\partial \hat{d}} - \frac{\partial F_2}{\partial \hat{x}_1}\frac{\partial F_1}{\partial \hat{d}}\right) \tag{79}$$

$$a_3 = (I_{L_1} + n^2 I_{L_2})\frac{\partial F_2}{\partial \hat{x}_3} + n^2 C_{12}\left(\frac{\partial F_1}{\partial \hat{x}_1}\frac{\partial F_2}{\partial \hat{d}} - \frac{\partial F_2}{\partial \hat{x}_1}\frac{\partial F_1}{\partial \hat{d}}\right) + C_3 R_{C_3}\left((1-D)\left(\frac{\partial F_1}{\partial \hat{x}_3}\frac{\partial F_2}{\partial \hat{d}} - \frac{\partial F_2}{\partial \hat{x}_3}\frac{\partial F_1}{\partial \hat{d}}\right) - (I_{L_1} + I_{L_2})\frac{\partial F_1}{\partial \hat{x}_1}\frac{\partial F_2}{\partial \hat{x}_3}n^2 + (I_{L_1} + n^2 I_{L_2})\frac{\partial F_1}{\partial \hat{x}_3}\frac{\partial F_2}{\partial \hat{x}_1}\right) \tag{80}$$

$$a_4 = (1-D)\left(\frac{\partial F_1}{\partial \hat{x}_3}\frac{\partial F_2}{\partial \hat{d}} - \frac{\partial F_2}{\partial \hat{x}_3}\frac{\partial F_1}{\partial \hat{d}}\right) + (I_{L_1} + n^2 I_{L_2})\left(\frac{\partial F_1}{\partial \hat{x}_3}\frac{\partial F_2}{\partial \hat{x}_1} - \frac{\partial F_1}{\partial \hat{x}_1}\frac{\partial F_2}{\partial \hat{x}_3}\right) \quad (81)$$

$$b_1 = -n^2 C_3 C_{12} L_f \quad (82)$$

$$b_2 = n^2 C_3 C_{12}\left(L_f\left(\frac{\partial F_1}{\partial \hat{x}_1} + \frac{\partial F_2}{\partial \hat{x}_2}\right) - R_f - R_{C_3}\right) \quad (83)$$

$$b_3 = C_3 L_f \frac{\partial F_1}{\partial \hat{x}_3} - C_{12} n^2 + C_{12} L f \frac{\partial F_2}{\partial \hat{x}_4} n^2 - C_3 D L_f \frac{\partial F_1}{\partial \hat{x}_3} - C_3 D L_f \frac{\partial F_2}{\partial \hat{x}_3} n^2 + C_3 C_{12}\Bigg(n^2 (R_{C_3} + R_f)\left(\frac{\partial F_1}{\partial \hat{x}_1} + \frac{\partial F_2}{\partial \hat{x}_2}\right) + n^2 R_{C_3}\frac{\partial F_2}{\partial \hat{x}_5} - n^2 L_f\left(\frac{\partial F_1}{\partial \hat{x}_1}\frac{\partial F_2}{\partial \hat{x}_2} - \frac{\partial F_1}{\partial \hat{x}_2}\frac{\partial F_2}{\partial \hat{x}_1}\right)\Bigg) \quad (84)$$

$$b_4 = C_3 (R_{C_3} + R_f)\frac{\partial F_1}{\partial \hat{x}_3} + n^2 C_{12}\Bigg(\frac{\partial F_1}{\partial \hat{x}_1} + \frac{\partial F_2}{\partial \hat{x}_2} + \frac{\partial F_2}{\partial \hat{x}_5} + R_f\frac{\partial F_2}{\partial \hat{x}_4}\Bigg) + C_3 L_f\left(\frac{\partial F_1}{\partial \hat{x}_2}\frac{\partial F_2}{\partial \hat{x}_3} - \frac{\partial F_1}{\partial \hat{x}_3}\frac{\partial F_2}{\partial \hat{x}_2}\right) - n^2 C_{12} L_f\left(\frac{\partial F_1}{\partial \hat{x}_1}\frac{\partial F_2}{\partial \hat{x}_4} - \frac{\partial F_1}{\partial \hat{x}_4}\frac{\partial F_2}{\partial \hat{x}_1}\right) + C_3 D\Bigg(-n^2 (R_{C_3} + R_f)\frac{\partial F_2}{\partial \hat{x}_3} - (R_{C_3} + R_f)\frac{\partial F_1}{\partial \hat{x}_3}\Bigg) - C_3 D L_f\Bigg(\frac{\partial F_2}{\partial \hat{x}_3}\Bigg(\frac{\partial F_1}{\partial \hat{x}_2} - n^2\frac{\partial F_1}{\partial \hat{x}_1}\Bigg) - \frac{\partial F_1}{\partial \hat{x}_3}\Bigg(\frac{\partial F_2}{\partial \hat{x}_2} - n^2\frac{\partial F_2}{\partial \hat{x}_1}\Bigg)\Bigg) - n^2 C_3 C_{12} R_f\left(\frac{\partial F_1}{\partial \hat{x}_1}\frac{\partial F_2}{\partial \hat{x}_2} - \frac{\partial F_1}{\partial \hat{x}_2}\frac{\partial F_2}{\partial \hat{x}_1}\right) - n^2 C_3 C_{12} R_{C_3}\Bigg(\frac{\partial F_1}{\partial \hat{x}_1}\Bigg(\frac{\partial F_2}{\partial \hat{x}_2} + \frac{\partial F_2}{\partial \hat{x}_5}\Bigg) - \frac{\partial F_2}{\partial \hat{x}_1}\left(\frac{\partial F_1}{\partial \hat{x}_2} - \frac{\partial F_1}{\partial \hat{x}_5}\right)\Bigg) \quad (85)$$

$$b_5 = (1-D)\frac{\partial F_1}{\partial \hat{x}_3} - n^2 D\frac{\partial F_2}{\partial \hat{x}_3} - n^2 C_{12}\Bigg(\frac{\partial F_1}{\partial \hat{x}_1}\frac{\partial F_2}{\partial \hat{x}_2} - \frac{\partial F_1}{\partial \hat{x}_2}\frac{\partial F_2}{\partial \hat{x}_1} + \frac{\partial F_1}{\partial \hat{x}_1}\frac{\partial F_2}{\partial \hat{x}_5} - \frac{\partial F_1}{\partial \hat{x}_5}\frac{\partial F_2}{\partial \hat{x}_1}\Bigg) - (1-D) L_f\left(\frac{\partial F_1}{\partial \hat{x}_3}\frac{\partial F_2}{\partial \hat{x}_4} - \frac{\partial F_1}{\partial \hat{x}_4}\frac{\partial F_2}{\partial \hat{x}_3}\right) + C_3 R_{C_3}(1-D)\left(-\frac{\partial F_1}{\partial \hat{x}_3}\frac{\partial F_2}{\partial \hat{x}_5} + \frac{\partial F_1}{\partial \hat{x}_5}\frac{\partial F_2}{\partial \hat{x}_3}\right) + C_3 (1-D)(R_f + R_{C_3})\left(\frac{\partial F_1}{\partial \hat{x}_2}\frac{\partial F_2}{\partial \hat{x}_3} - \frac{\partial F_1}{\partial \hat{x}_3}\frac{\partial F_2}{\partial \hat{x}_2}\right) + n^2 C_3 D R_{C_3}\left(\frac{\partial F_1}{\partial \hat{x}_1}\frac{\partial F_2}{\partial \hat{x}_3} - \frac{\partial F_1}{\partial \hat{x}_3}\frac{\partial F_2}{\partial \hat{x}_1}\right) - C_3 D R_f\left(-\frac{\partial F_1}{\partial \hat{x}_1}\frac{\partial F_2}{\partial \hat{x}_3} n^2 + \frac{\partial F_1}{\partial \hat{x}_3}\frac{\partial F_2}{\partial \hat{x}_1} n^2\right) - n^2 C_{12} R_f\left(\frac{\partial F_1}{\partial \hat{x}_1}\frac{\partial F_2}{\partial \hat{x}_4} - \frac{\partial F_1}{\partial \hat{x}_4}\frac{\partial F_2}{\partial \hat{x}_1}\right) \quad (86)$$

$$b_6 = (1-D)\left(\frac{\partial F_2}{\partial \hat{x}_3}\left(\frac{\partial F_1}{\partial \hat{x}_2} + \frac{\partial F_1}{\partial \hat{x}_5}\right) - \frac{\partial F_1}{\partial \hat{x}_3}\left(\frac{\partial F_2}{\partial \hat{x}_2} + \frac{\partial F_2}{\partial \hat{x}_5}\right)\right) - R_f(1-D)\left(\frac{\partial F_1}{\partial \hat{x}_3}\frac{\partial F_2}{\partial \hat{x}_4} - \frac{\partial F_1}{\partial \hat{x}_4}\frac{\partial F_2}{\partial \hat{x}_3}\right) + n^2 D\left(\frac{\partial F_1}{\partial \hat{x}_1}\frac{\partial F_2}{\partial \hat{x}_3} - \frac{\partial F_1}{\partial \hat{x}_3}\frac{\partial F_2}{\partial \hat{x}_1}\right) \quad (87)$$

$$c_1 = C_3 C_{12} L_1 R_f V_g n^3 (D-1) \quad (88)$$

$$c_2 = L_1 n^3 (C_3 R_{C_3} I_{L_f} D^2 + C_{12} V_g D - C_{12} V_g) \quad (89)$$

$$c_3 = L_1 I_{L_f} D^2 n^3 - C_3 R_{C_3} V_g (D-1)^2 \quad (90)$$

$$c_4 = -V_g (D-1)^2 \quad (91)$$

$$e_1 = C_3 C_{12} L_1 L_2 L_f D n^3 (D-1) \quad (92)$$

$$e_2 = D(D-1) C_{12} C_3 L_1 n^3 (L_2 R_{C_3} + L_2 R_f + L_f R_{C_3}) \quad (93)$$

$$e_3 = D(D-1)(C_3 L_2 L_f + C_{12} L_1 L_2 n^3 + C_{12} L_1 L_f n^3 - 2C_3 L_2 L_f D + C_3 L_2 L_f D^2 + C_3 L_1 L_f D^2 n^3 + C_3 C_{12} L_1 R_{C_3} R_f n^3) \quad (94)$$

$$e_4 = D(D-1)(C_3 L_2 R_{C_3} + C_3 L_2 R_f + C_3 L_f R_{C_3} + C_3 L_2 R_f D^2 + C_3 L_2 R_f D^2 + C_3 L_f R_{C_3} D^2 + C_{12} L_1 R_f n^3 - 2C_3 L_2 R_{C_3} D - 2C_3 L_2 R_f D - 2C_3 L_f R_{C_3} D + C_3 L_1 R_{C_3} D^2 n^3 + C_3 L_1 R_f D^2 n^3) \quad (95)$$

$$e_5 = D(D-1)(L_2 + L_f - 2L_2 D - 2L_f D + L_2 D^2 + L_f D^2 + L_1 D^2 n^3 + C_3 R_{C_3} R_f + C_3 R_{C_3} R_f D^2 - 2C_3 R_{C_3} R_f D) \quad (96)$$

$$e_6 = D(D-1)^3 R_f \quad (97)$$

$$f_1 = T_s^2 (a_4 T_s^3 + a_3 T_s^2 + a_2 T_s + a_1) \quad (98)$$

$$f_2 = -T_s^2 (a_3 T_s^2 + 2a_2 T_s + 3a_1) \quad (99)$$

$$f_3 = T_s^2 (3a_1 + T_s a_2) \quad (100)$$

$$f_4 = -T_s^2 a_1 \quad (101)$$

$$g_1 = b_6 T_s^5 + b_5 T_s^4 + b_4 T_s^3 + b_3 T_s^2 + b_2 T_s + b_1 \quad (102)$$

$$g_2 = -b_5 T_s^4 - 2b_4 T_s^3 - 3b_3 T_s^2 - 4b_2 T_s - 5b_1 \quad (103)$$

$$g_3 = b_4 T_s^3 + 3b_3 T_s^2 + 6b_2 T_s + 10b_1 \quad (104)$$

$$g_4 = -b_3 T_s^2 - 4b_2 T_s - 10b_1 \quad (105)$$

$$g_5 = 5b_1 + T_s b_2 \quad (106)$$

$$g_6 = -b_1 \quad (107)$$

$$l_1 = T_s^2 (c_4 T_s^3 + c_3 T_s^2 + c_2 T_s + c_1) \quad (108)$$

$$l_2 = -T_s^2 (c_3 T_s^2 + 2c_2 T_s + 3c_1) \quad (109)$$

$$l_3 = T_s^2 (3c_1 + T_s c_2) \quad (110)$$

$$l_4 = -T_s^2 c_1 \quad (111)$$

$$m_1 = e_6 T_s^5 + e_5 T_s^4 + e_4 T_s^3 + e_3 T_s^2 + e_2 T_s + e_1 \quad (112)$$

$$m_2 = -e_5 T_s^4 - 2e_4 T_s^3 - 3e_3 T_s^2 - 4e_2 T_s - 5e_1 \quad (113)$$

$$m_3 = e_4 T_s^3 + 3e_3 T_s^2 + 6e_2 T_s + 10e_1 \quad (114)$$

$$m_4 = -e_3 T_s^2 - 4e_2 T_s - 10e_1 \quad (115)$$

$$m_5 = 5e_1 + T_s e_2 \quad (116)$$

$$m_6 = -e_1. \quad (117)$$

ACKNOWLEDGMENT

The authors would like to thank Dr. J. S. Lee for his assistance in this paper.

REFERENCES

[1] L. Chen, A. Amirahmadi, Q. Zhang, N. Kutkut, and I. Batarseh, "Design and implementation of three-phase two-stage grid-connected module integrated converter," *IEEE Trans. Power Electron.*, vol. 29, no. 8, pp. 3881–3892, Aug. 2014.

[2] M. Mirjafari, S. Harb, and R. Balog, "Multiobjective optimization and topology selection for a module-integrated inverter," *IEEE Trans. Power Electron.*, vol. 30, no. 8, pp. 4219–4231, Aug. 2015.

[3] R. Y. Kim and J. S. Lai, "A seamless mode transfer maximum power point tracking controller for thermoelectric generator applications," *IEEE Trans. Power Electron.*, vol. 23, no. 5, pp. 2310–2318, May 2008.

[4] B. York, W. Yu, and J. S. Lai.,"An integrated boost resonant converter for photovoltaic applications," *IEEE Trans. Power Electron.*, vol. 28, no. 3, pp. 1199–1207, Mar. 2013.

[5] T. LaBella, W. Yu, J. S. Lai, M. Senesky, and D. Anderson, "A bidirectional-switch-based wide-input range high-efficiency isolated resonant converter for photovoltaic applications," *IEEE Trans. Power Electron.*, vol. 29, no. 7, pp. 3473–3484, Jul. 2014.

[6] S. Harb and R. S. Balog, "Reliability of candidate photovoltaic module-integrated-inverter (PV-MII) topologies-a usage model approach," *IEEE Trans. Power Electron.*, vol. 29, no. 6, pp. 3019–3027, Jun. 2013.

[7] M. Gao, M. Chen, C. Zhang, and Z. Qian, "Analysis and implementation of an improved flyback inverter for photovoltaic AC module applications," *IEEE Trans. Power Electron.*, vol. 29, no. 7, pp. 3428–3444, Jul. 2014.

[8] Z. Zhang, M. Chen, W. Chen, C. Jiang, and Z. Qian, "Analysis and implementation of phase synchronization control strategies for BCM interleaved flyback microinverters," *IEEE Trans. Power Electron.*, vol. 29, no. 11, pp. 5921–5932, Nov. 2014.

[9] G. C. Christidis, A. C. Nanakos, and E. C. Tatakis, "Hybrid discontinuous/boundary conduction mode of flyback microinverter for ACPV modules," *IEEE Trans. Power Electron.*, vol. 31, no. 6, pp. 4195–4205, Jun. 2016.

[10] H. Kim, J. S. Lee, J. S. Lai, and M. Kim, "Iterative learning controller with multiple phase-lead compensation for dual-mode flyback inverter," *IEEE Trans. Power Electron.*, vol. 32, no. 8, pp. 6468–6480, Aug. 2017.

[11] H. Kim, J. S. Lee, and M. Kim, "Down-sampled iterative learning controller for flyback CCM inverter," *IEEE Trans. Ind. Electron.*, vol. 65, no. 1, pp. 510–520, Jan. 2018.

[12] C. Pan, M. Cheng, and C. Lai, "A novel integrated DC/AC converter with high voltage gain capability for distributed energy resource systems," *IEEE Trans. Power Electron.*, vol. 27, no. 5, pp. 2385–2395, May 2012.

[13] B. Han, M. Kim, S. H. Lee, and J. S. Lee, "Dynamic modeling and integral sliding mode controller design for the Cuk inverter," in *Proc. 17th Eur. Conf. Power Electron. Appl.*, Sep. 2015, pp. 1–9.

[14] A. Darwish, D. Holliday, S. Ahmed, A. M. Massoud, and B. W. Williams, "A single-stage three-phase inverter based on Cuk converters for PV applications," *IEEE Trans. Emerg. Sel. Topics Power Electron.*, vol. 2, no. 4, pp. 797–807, Apr. 2014.

[15] A. Diab-Marzouk and O. Trescases, "SiC-based bidirectional Cuk converter with differential power processing and MPPT for a solar powered aircraft," *IEEE Trans. Transport. Electrific*, vol. 1, no. 4, pp. 369–381, Apr. 2015.

[16] Texas Instruments, Inc., "Improving the performance of traditional flyback topology with two-switch approach," Texas Instruments, Inc., Dallas, TX, USA, Appl. Rep. SNVA716, Jul. 2014.

[17] J. Knight, S. Shirsavar, and W. Holderbaum, "An Improved reliability Cuk based solar inverter with sliding mode control," *IEEE Trans. Power Electron.*, vol. 21, no. 4, pp. 1107–1115, Jul. 2006.

[18] S. Mehrnami and S. K. Mazumder, "Discontinuous modulation scheme for a differential-mode Cuk inverter," *IEEE Trans. Power Electron.*, vol. 30, no. 3, pp. 1242–1254, Mar. 2015.

[19] H. Yang, H. Chiang, and C. Chen, "Implementation of bridgeless Cuk power factor corrector with positive output voltage," *IEEE Trans. Ind. Appl.*, vol. 51, no. 4, pp. 3325–3333, Jul./Aug. 2015.

[20] S. Mehrnami, S. K. Mazumder, and H. Soni, "Modulation scheme for three-phase differential-mode Cuk inverter," *IEEE Trans. Power Electron.*, vol. 31, no. 3, pp. 2654–2668, Mar. 2016.

[21] V. Gautam and P. Sensarma, "Design of Cuk derived transformerless common grounded PV micro-inverter in CCM," *IEEE Trans. Ind. Electron.*, vol. 64, no. 8, pp. 6245–6254, Aug. 2017.

[22] E. Arango, C. A. Ramos-Paja, R. Giral, S. Serna, and G. Petrone, "Modeling and control of Cuk converter operating in DCM," in *Electrical Engineering and Control* (Lecture Notes in Electrical Engineering), vol. 98. Berlin, Germany: Springer, 2011, pp. 441–449.

[23] G. M. Soares, P. S. Almeida, D. P. Pinto, and H. A. C. Braga, "A single-stage high efficiency long-life off-line LED driver based on the DCM Cuk converter," in *Proc. 38th Annu. Conf. Ind. Electron. Soc.*, Oct. 25–28, 2012, pp. 4509–4514.

[24] D. S. L. Simonetti, J. Sebastian, and J. Uceda, "The discontinuous conduction mode Sepic and Cuk power factor preregulators: Analysis and design," *IEEE Trans. Ind. Electron.*, vol. 44, no. 5, pp. 630–637, Oct. 1997.

[25] G. Ranganathan and L. Umanand, "Power factor improvement using DCM Cuk converter with coupled inductor," in *Proc. Inst. Elect. Eng. Elect. Power Appl. Conf.*, 1999, pp. 231–236.

[26] H. Wirth, *Recent Facts About Photovoltaics in Germany*. Freiburg, Germany: Fraunhofer Inst., 2015. Available at: http://www.ise.fraunhofer.de/en/renewable-energy-data

[27] X. F. Zheng, C. X. Liu, Y. Y. Yan, and Q. Wang, "A review of thermoelectrics research—Recent developments and potentials for sustainable and renewable energy applications," *Renewable Sustain. Energy Rev.*, vol. 32, pp. 486–503, Apr. 2014.

[28] J. Tsai, C. Chen, Y. Lee, H. Yang, M. Hsu, and K. Chen, "Modified hysteretic current control (MHCC) for improving transient response of boost converter," *IEEE Trans. Circuits Syst. I, Reg. Papers*, vol. 58, no. 8, pp. 1967–1979, Aug. 2011.

[29] Y. Jia, J. Zhao, and X. Fu, "Direct grid current control of LCL-filtered grid-connected inverter mitigating grid voltage disturbance," *IEEE Trans. Power Electron.*, vol. 29, no. 3, pp. 1532–1541, Mar. 2014.

[30] Y. Wang, B. Ren, and Q. Zhong, "Robust power flow control of grid-connected inverters," *IEEE Trans. Ind. Electron.*, vol. 63, no. 11, pp. 6887–6897, Nov. 2016.

[31] Y. Cho and J. Lai, "Digital plug-in repetitive controller for single-phase bridgeless PFC converters," *IEEE Trans. Power Electron.*, vol. 28, no. 1, pp. 165–175, Jan. 2013.

[32] S. H. Lee, W. J. Cha, B. H. Kwon, and M. Kim, "Discrete-time repetitive control of flyback CCM inverter for PV power applications," *IEEE Trans. Ind. Electron.* vol. 63, no. 2, pp. 976–984, Feb. 2016.

[33] Y. Wang, A. Darwish, D. Holliday, and B. W. Williams, "Plug-in repetitive control strategy for high-order wide-output range impedance-source converters," *IEEE Trans. Power Electron.*, vol. 32, no. 8, pp. 6510–6522, Aug. 2017.

[34] S. Yang, P. Wang, Y. Tang, and L. Zhang, "Explicit phase lead filter design in repetitive control for voltage harmonic mitigation of VSI-based islanded microgrids," *IEEE Trans. Ind. Electron*, vol. 64, no. 1, pp. 817–826, Jan. 2017.

[35] Y. Ye, Y. Wu, G. Xu, and B. Zhang, "Cyclic repetitive control of CVCF PWM DC-AC converters," *IEEE Trans. Ind. Electron.*, vol. 64, no. 12, pp. 9399–9409, Dec. 2017.

[36] E. D. Hagh, P. Mohammadalizadeh, and E. Babaei, "Effects of ESR on stability and frequency response of Cuk converter by using signal flow graph method," in *Proc. 2015 6th Power Electron., Drives Syst. Technol. Conf.*, 2015, pp. 83–88.

[37] G. F. Franklin, J. D. Powell, and M. Workman, *Digital Control of Dynamic Systems*, vol. 3. Reading, MA, USA: Addison-Wesley, 1997.

[38] D. Wang and Y. Ye, "Design and experiments of anticipatory learning control: Frequency domain approach," *IEEE/ASME Trans. Mechatronics*, vol. 10, no. 3, pp. 305–313, Jun. 2005.
[39] B. Zhang, D. Wang, K. Zhou, and Y. Wang, "Linear phase lead compensation repetitive control of a CVCF PWM inverter," *IEEE Trans. Ind. Electron.*, vol. 55, no. 4, pp. 1595–1602, Apr. 2008.
[40] U. Aridogan, Y. Shan, and K. K. Leang, "Design and analysis of discrete-time repetitive control for scanning probe microscopes," *ASME, J. Dyn. Syst. Meas. Control*, vol. 131, no. 6, Nov. 2009, Art. no. 061103.

Byeongcheol Han (S'15) was born in Busan, South Korea, in 1986. He received the B.S degree in electrical engineering from Pusan National University, Busan, South Korea, in 2012. He is currently working toward the Ph.D. degree in creative IT engineering (CiTE) at Pohang University of Science and Technology (POSTECH), Pohang, South Korea.

His research interests include nonlinear systems and control, grid-connected inverters, energy storage systems, and controller design for power conversion systems.

Jih-Sheng (Jason) Lai (S'85–M'89–SM'93–F'07) received the M.S. and Ph.D. degrees in electrical engineering from the University of Tennessee, Knoxville, TN, USA, in 1985 and 1989, respectively.

In 1989, he joined the Electric Power Research Institute (EPRI) Power Electronics Applications Center, where he managed EPRI-sponsored power electronics research projects. In 1993, he then joined the Oak Ridge National Laboratory as the Power Electronics Lead Scientist, where he initiated a high-power electronics program and developed several novel high-power converters including multilevel converters and soft-switching inverters. In 1996, he joined the Virginia Polytechnic Institute and State University. He is currently the James S. Tucker Professor with the Electrical and Computer Engineering Department and the Director for Future Energy Electronics Center. He also holds Honorary International Chair Professorship with the National Taipei University of Technology, Taipei, Taiwan, and serves as a Visiting Professor with Nanyang Technological University, Singapore. He has authored/coauthored more than 360 refereed technical papers and 2 books and has 25 U.S. patents. His research interests include high-efficiency power electronics conversions for high power and energy applications.

Dr. Lai was the recipient of the Technical Achievement Award in Lockheed Martin Award Night, 2 Journal Paper Awards, 11 Best Paper Awards from IEEE sponsored conferences, the Virginia Tech Deans Award on research excellence, and the 2016 IEEE IAS Gerald Kliman Innovator Award. He led the student teams to win top three finalist in the Google Little Box Challenge in 2016, the Grand Prize Award from the International Future Energy Challenge in 2011, the Grand Prize Award in the Texas Instruments Engibous Analog Design Competition in 2009. He is the Founding Chair for the 2001 IEEE Future Energy Challenge and 2016 IEEE Asian Conference on Energy, Power, and Transportation Electrification and the General Chair of IEEE Workshop on Computers in Power Electronics (COMPEL 2000) and IEEE Applied Power Electronics Conference and Exposition (APEC 2005).

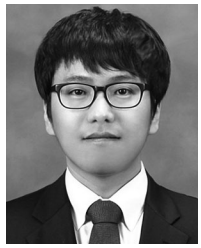

Minsung Kim (M'14) was born in Ulsan, Korea, in 1986. He received the B.S. degree in electrical engineering from Pohang University of Science and Technology (POSTECH), Pohang, Korea, in 2008, and the Ph.D. degree in electrical engineering from POSTECH, Pohang, Korea, in 2013.

Since 2013, he has been with Department of Creative IT Engineering and Future IT Research Laboratory, POSTECH, Pohang, Korea, where he is currently Research Assistant Professor. In 2016, he has also worked as Research Scholar in Future Energy Electronics Center at Virginia Tech, Blacksburg, VA. In 2017, he has also served as Academic Visitor in Control and Power System Group at Imperial College London, London, UK. Since 2018, he has been with the Division of Electronics and Electrical Engineering, Dongguk University, Seoul, Korea, where he is currently an Assistant Professor. His current research interests include highly efficient power conversion circuit design, intelligent controller design for industrial electronics, and renewable energy and energy storage systems.